


Radish concretions grown in mud during compaction

ANDREAS WETZEL*  and MACIEJ BOJANOWSKI† 

*Departement Umweltwissenschaften – Geologie, Universität Basel, Bernoullistrasse 32, CH-4056, Basel Switzerland (E-mail: andreas.wetzel@unibas.ch)

†Institute of Geological Sciences of the Polish Academy of Sciences, Twarda 51/55, PL-00-818, Warsaw Poland

Associate Editor – Jim Hendry

ABSTRACT

Radish concretions exhibit a typical columnar to pear-shaped, stipe downward geometry. In Middle Jurassic mudrock in south-west Germany, radish concretions started to form around an iron-sulphide lined tube by pervasive cementation constituting an ellipsoidal parent domain in uncompacted sediment at burial depths of ≤ 5 to 8 m as recorded by 75 to 80% minus-cement porosity. Thereafter, the concretions grew vertically in compacting sediment as evidenced by laminae within the concretions being increasingly inclined towards the tips, and concomitantly decreasing minus-cement porosity. During early diagenesis, prior to septarian crack formation, bicarbonate generating the microbial cement originated within the sulphate reduction zone chiefly from anaerobic oxidation of methane and to a lesser degree of organoclastic material. Later, at 50 to 70 m burial depth, septarian cracks formed as evaluated by sedimentation–compaction analysis based on minus-cement porosity data and compressibility of similarly composed sediments. The outward-narrowing septarian cracks indicate that they formed when the concretions were still in a plastic state but already cemented sufficiently to be resistant against compaction. In this stage, up to one-quarter of the pore volume of the concretions was still open as suggested by shrinkage experiments. This pore volume, and the septarian cracks, were filled with cement termed late diagenetic. In the study area, the decompacted net-sedimentation rate was low, about 2 to 3 cm kyr⁻¹, for ca 2.5 Myr, allowing the concretions to reside for a long time within the sulphate reduction zone and to grow. Radish concretions formed within the transition zone from thick, rapidly deposited to long-term, slowly accumulating sediment.

Keywords Anaerobic oxidation of methane, burial history, concretion, mudrock, sedimentary hiatus.

INTRODUCTION

Early diagenetic concretions have attracted geologists for a long time because they represent containers resistant to compaction and, therefore, they may preserve the initial sediment fabric, primary and bioturbational sedimentary structures, as well as fossils in three dimensions (e.g. Oertel & Curtis, 1972; Blome & Albert, 1985; Allison & Pye, 1994; Wetzels & Reisdorf,

2007; Day-Stirrat *et al.*, 2008; Hall & Savrda, 2008; Lash, 2018). To evaluate the onset of concretion growth, minus-cement porosity is usually determined (e.g. Lippmann, 1955; Šrámek, 1978; Lash & Blood, 2004). Concretions may form at wide burial depth ranges and therefore can record geochemical conditions in the diagenetic environment during their formation (e.g. Hudson, 1978; Coleman & Raiswell, 1993; Bojanowski *et al.*, 2014). Furthermore, the chemical

composition and petrography of cement preserves information about depositional and diagenetic environments (e.g. Mozley & Burns, 1993). It has also been suggested that the shape of the concretions is roughly controlled by permeability and porosity of the host sediment (e.g. Sellés-Martinez, 1996; and references therein; Seilacher, 2001). In uncompacted, isotropic sediments, spherical concretions can grow during early diagenesis, whereas in already compacted and/or laminated mudstone, ellipsoidal concretions develop because solute transfer and diffusion are optimized parallel to lamination.

Concretions may form due to *pervasive* cementation of a rather constant sediment volume or *concentric outward* growth by the successive radial addition of cement layers that were successively sealed off from each other and from the surroundings (e.g. Mozley, 1996; Raiswell & Fisher, 2000). The presence of outward-narrowing septarian cracks is taken as evidence of internal shrinkage of the forming concretion and implies that growing concretions were still in a plastic state and incompletely lithified prior to crack formation, and hence that subsequent cement could precipitate in the concretion at a later stage (e.g. Wetzel, 1992; Hudson *et al.*, 2001; Hendry *et al.*, 2006; Loyd & Berelson, 2016). The initially formed cement makes the initial concretion bodies resistant to compaction but they still lack rigidity, otherwise the formation of outward-narrowing cracks would be geometrically impossible (Wetzel, 1992). In fact, only partially lithified concretions have been encountered a few metres below the sediment surface at a modern methane seep site (Franchi *et al.*, 2017). In contrast, bored and encrusted early diagenetic concretions imply a more rapid and complete cementation (e.g. Hesselbo & Palmer, 1992; Wetzel & Allia, 2000; Zatoń *et al.*, 2011). During exhumation however, carbonate precipitation might have been enhanced due to the alkaline conditions produced by degrading (microbial) amino acids within the concretions (cf. Duck, 1995).

For concretions grown during compaction and having a columnar to elongate, roughly axially symmetrical shape, Seilacher (2001) introduced the term 'radish concretions'. So far, only a few studies have addressed concretions exhibiting such a shape (e.g. Durga Prasada Rao *et al.*, 1982; Melezhik *et al.*, 2007; Leonowicz, 2015). In contrast, elongate concretions that formed in association with fluid conduits at methane seep sites are more frequently described (e.g. de

Boever *et al.*, 2006; Nyman *et al.*, 2010). Seilacher (2001) invoked burrows to explain the shape of radish concretions; these findings relied on detailed macroscopic observations and investigative comparisons with concretions of various morphologies, but Seilacher did not study either the concretions' internal structure or geochemistry.

The aims of this paper are: (i) to analyze radish concretions with respect to their shape and internal structure; (ii) to decipher the meaning of their geometry; (iii) to determine cement volumes and bulk carbon and oxygen isotope compositions; (iv) to characterize the diagenetic environment in which they formed; (v) to interpret their growth history and the influencing factors; and (vi) to discuss the sedimentological significance of radish concretions.

GEOLOGICAL SETTING

Radish concretions of this study were found in Middle Jurassic mudrock from south-west Germany (Fig. 1). During the Mesozoic, the study area formed part of an epicontinental basin system that developed in central Europe (e.g. Ziegler, 1990). In the study area, subsidence and deposition started during the early Triassic;

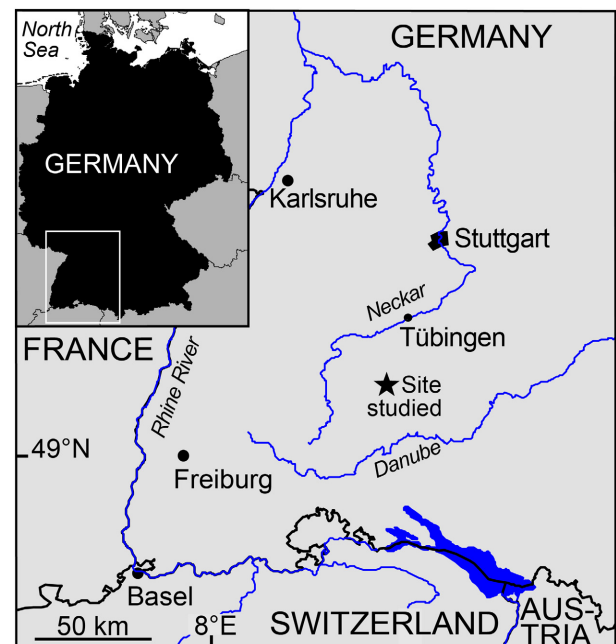


Fig. 1. Location of the study area in south-west Germany.

until the late Early Jurassic, no deposits accumulated that could act as hydrocarbon source rocks (e.g. Geyer & Gwinner, 2011). The radish concretions occur in mudrock of the upper part of the Opalinuston Formation that formed during the Aalenian in the southern part of the central European epicontinental basin, with two-thirds to three-quarters of the basin surrounded by land (e.g. Ziegler, 1990; Franz & Nitsch, 2009). During the Aalenian opalinum Zone, which lasted *ca* 1.2 Myr (Hardenbol *et al.*, 1998), the *ca* 120 m thick uniform, greyish, mudrock of the Opalinuston Formation, which is characterized by a variable sand content and intercalated sandstone beds, accumulated at an average decompacted sedimentation rate of *ca* 30 to 40 cm kyr⁻¹ (e.g. Wetzel & Allia, 2003). Due to palaeogeography and large freshwater inflow from the adjacent land, the seafloor was poorly oxygenated except during periods of enhanced current activity (e.g. Schmidt, 1996; Wetzel & Allia, 2003). Bioturbational structures with indistinct outlines and produced close to the sediment surface are typical of these settings (e.g. Wetzel *et al.*, 2011; Campetella *et al.*, 2020). The Opalinuston Formation contains 0.5 to 2.0% C_{org} (e.g. Elie & Mazurek, 2008).

Depositional water depth was around storm-wave base or somewhat below, as indicated by hummocky cross-stratification, long wave length sandstone ripples, exhumed, encrusted and bored concretions, and crinoid lagerstätten covered by storm sand (Wetzel & Allia, 2000; Wetzel & Allia, 2003; Wetzel & Meyer, 2006). Tempestites have been calculated to be deposited in about 30 to 40 m water depth based on amplitude, wavelength and grain size of ripples (Allia, 1996).

At the end of the opalinum Zone, the subsidence rate decreased allowing for repeated sediment reworking that is documented by an increasing number of erosively-based sandstone beds and a concomitant upward increasing sand content towards the so-called Wasserfall beds and the calcareous Wilflingen Bed (previously Comptum Bed; Dietze *et al.*, 2021), which locally contains exhumed, bored and encrusted concretions. During accumulation of the overlying Achdorf Formation, sediment reworking, omission and erosion continued and caused an overall low net-sediment aggradation rate of <5 cm kyr⁻¹ (Fig. 2; Franz & Nitsch, 2009; Geyer & Gwinner, 2011).

Sedimentation continued at least until the Late Jurassic and very likely into the Early

Cretaceous, but with latter deposits subsequently removed by erosion, as suggested by one-dimensional basin modelling and evaluation of the thermal history for several deep drill holes in northern Switzerland, about 50 to 80 km to the south of the study area (for details see Mazurek *et al.*, 2006; Villagómez-Díaz *et al.*, 2021). Based on this modelling, the Opalinuston Formation experienced a maximum burial temperature of about 75 to 85°C (Mazurek *et al.*, 2006; Elie & Mazurek, 2008).

Through the early Aalenian, the isotope composition of seawater in Eurasian epicontinental seas showed an increase for $\delta^{18}\text{O}$ from $-1.5 \pm 0.5\text{‰}$ to $-0.5 \pm 0.5\text{‰}$ Vienna Standard Mean Ocean Water (V-SMOW) and an increase for $\delta^{13}\text{C}$ of dissolved inorganic carbon (DIC) from $+1 \pm 0.5\text{‰}$ to $+2 \pm 1\text{‰}$ Vienna Pee Dee Belemnite (V-PDB; Dera *et al.*, 2011). For the purposes of calculations in this study, representative early Aalenian mean values used are -1‰ for $\delta^{18}\text{O}$ and $+1.5\text{‰}$ $\delta^{13}\text{C}$ (Dera *et al.*, 2011).

MATERIAL AND METHODS

Radish concretions were collected during 1981 at a road construction site 2 km south-west of the village of Zillhausen (south-west Germany; coordinates 48°14'54"N, 8°54'50"E). Thirty concretions, some of them in place, were collected from the Middle Jurassic Opalinuston Formation in a rather confined interval, about 3 to 4 m below the Wilflingen Bed (previously Comptum Bed, Dietze *et al.*, 2021; Fig. 2). Today, the outcrop is covered by pavement or overgrown by vegetation. The concretions described in this paper are stored at the Museum of Natural History (Basel, Switzerland).

Concretion size was measured and shape was determined. Their internal structures were studied on polished or etched surfaces. Four concretions were serially sectioned into 6 to 8 mm thick slices to calculate the volume of septarian cracks. Petrographic thin sections were examined via standard light microscopy and cold cathodoluminescence microscopy. Two systems were used: (i) the CITL Mark II; and (ii) the CITL Mk5-2 (Cambridge Image Technology, Cambridge, UK). Scanning electron microscopic (SEM) analyses were carried out on dried, polished samples sputter-coated with Au with a Philips ESEM 5000 (Philips, Eindhoven, The Netherlands) equipped with an X-ray energy-dispersive elemental analysis system (EDAX);

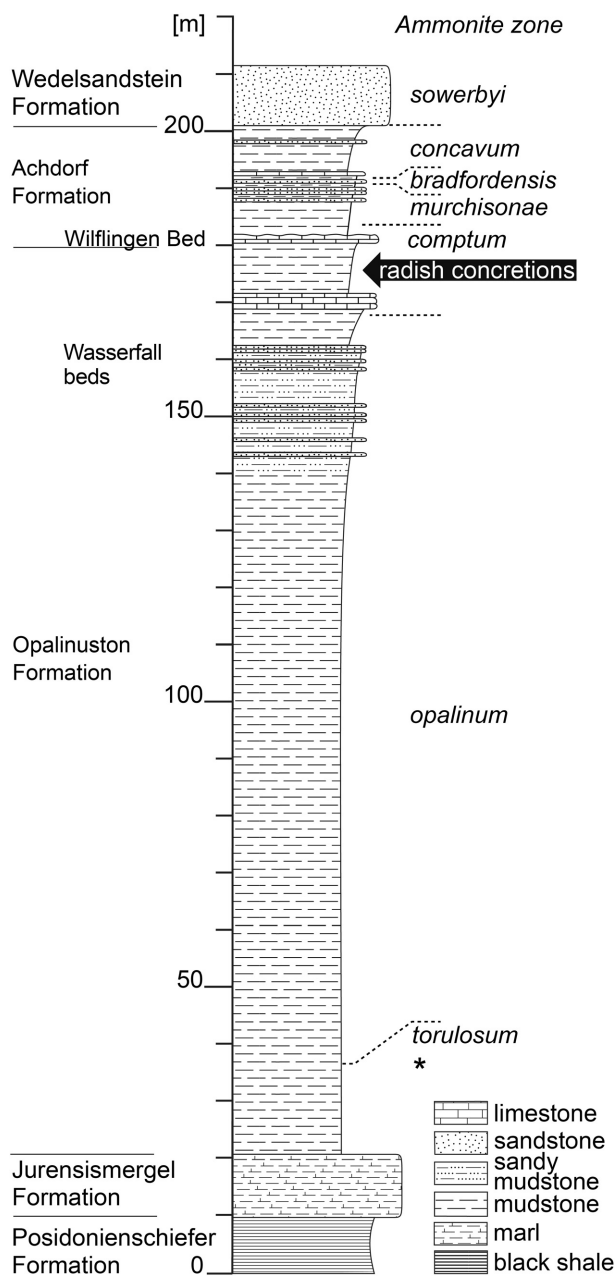


Fig. 2. Schematic stratigraphic section close to the studied site (after Geyer & Gwinner, 2011); interval housing the studied radish concretions marked by an arrow; * ammonite zones below the torulosum Zone are not shown.

and on thin sections sputter-coated with C by using a ZEISS Sigma Variable Pressure Field Emission SEM (Zeiss AG, Oberkochen, Germany) equipped with two Bruker XFlash 6110 SDD type detectors (Bruker Corporation, Billerica, MA, USA) for energy-dispersive analysis as well. All quantitative elemental data for

carbonates presented in this work were acquired with the field emission ZEISS Sigma SEM; the analyses were standardless, but the detection limit and the precision were *ca* 0.1 wt.% for the elements analyzed (Ca, Mg, Fe, Mn).

For mineral identification by X-ray diffraction (XRD), bulk powdered samples were put into an aluminium tray and analyzed with a Siemens D 5000 diffractometer (Siemens, Munich, Germany). Cu K α 1 radiation was used measuring 0.05 \cdot 2 θ steps for 25 min. The software package Diffracto plus (EVA and TOPAS) provided by Bruker Analytical X-Ray Systems was used for mineral identification.

Carbonate content was quantified on a Carmograph 6 (Wösthoff GmbH, Bochum, Germany) using calcite standards for calibration and 2N H₃PO₄ for sample acidification; the machine measures the amount of liberated CO₂ conductometrically. To quantify the amount of Ca and Mg, carbonate was dissolved in 1N HCl. The Ca and Mg of the solution were measured using inductively coupled plasma (ICP) mass spectrometry on the EOP SPETRO Ciros Vision spectrometer (Spectro Analytical Instruments, Kleve, Germany). Organic carbon was determined by measuring the carbon content of carbonate-free material on an Erba Science NA 1500 Elemental Analyzer (Carlo Erba Limited, Cambridge, UK).

Bulk samples for measurements of carbon and oxygen isotopes were taken by a dental drill from macroscopically defined domains on polished slabs. The isotopes were measured by a VG Isogas PRISM and a Gasbench II coupled to a Delta V Plus mass spectrometer (Thermo Fisher Scientific, Bremen, Germany). The carbon and oxygen isotopic compositions were calibrated against international carbonate isotope reference materials (NBS19, NBS18, LSVEC) and expressed as $\delta^{13}\text{C}$ and $\delta^{18}\text{O}$ in ‰ relative to V-PDB. Based on routine analyses of the carbonate isotope standards analytical precision was $\leq \pm 0.1\text{‰}$ for $\delta^{13}\text{C}$ and $\leq \pm 0.2\text{‰}$ for $\delta^{18}\text{O}$. For temperature calculation the empirical equation given by Anderson & Arthur (1983) was used.

Minus-cement porosity was calculated by subtracting the carbonate content of the host rock from that of a concretion sample and expressing it as porosity by using a density of 2.72 g cm⁻³ for calcite and 2.67 g cm⁻³ for siliciclastic material. For example, a given concretion contains 80% carbonate and occurs in a siliciclastic host sediment with grain density $\rho_s = 2.67 \text{ g cm}^{-3}$ containing 3.5% detrital carbonate (see *Results*; $\rho_s = 2.72 \text{ g cm}^{-3}$); subtracting the detrital carbonate from that of the

concretion, $80\% - 3.5\% = 76.5\%$, equals the cement content (= cement filled porosity) of the concretion. A 100 g sample of such concretion consists of 76.5 g of calcite cement that equals a volume of $76.5 \text{ g} : 2.72 \text{ g cm}^{-3} = 28.1 \text{ cm}^3$. The sediment within the 100 g concretion consists of 20 g of siliciclastic material representing $20 \text{ g} : 2.67 \text{ g cm}^{-3} = 7.5 \text{ cm}^3$ and of 3.5 g detrital carbonate representing $3.5 \text{ g} : 2.72 \text{ g cm}^{-3} = 1.3 \text{ cm}^3$, in total 8.8 cm^3 . The minus-cement porosity is cement volume – total volume, $28.1 - (28.1 + 8.8) = 0.76$ (or 76%).

The shrinkage limit giving the water content when mud changes from plastic to brittle behaviour was determined following the procedure given by the German Bureau of Standards (DIN 18122-2, 2000). Water is added to a completely disintegrated mud sample until saturation. Then it is dried at room temperature, and sample volume and weight are repeatedly recorded until volume loss ceases. Finally, the sample is dried for 24 h at 110°C . The shrinkage limit is given at the water content when the sample volume did not change any longer. The determinations were carried out on four completely disaggregated samples of the mudrock hosting the concretions in 1981. Supposedly, clay mineralogy was not severely affected by diagenesis because of the low temperature the Opalinuston mudrock experienced during burial (see above).

The burial history was evaluated by sedimentation–compression analysis quantifying the decrease of pore-volume with depth (e.g. Lee, 1973). Because the compressibility of mud correlates fairly well with its porosity near the sediment surface (= initial porosity (n_0); Rieke & Chilingarian, 1974; Wetzel, 1990; Hong *et al.*, 2020), the pore volume in burial depth d_x , expressed as void ratio e_x [$e = n/(1 - n)$ with porosity n given as decimal] can be calculated by using the equation:

$$e_x = e_0 - C_c \cdot \log_{10}(d_x/d_0) \quad (1)$$

wherein C_c is compression index and e_0 refers to the void ratio near the sediment surface in depth d_0 (e.g. Rieke & Chilingarian, 1974; Mitchell, 1993). The initial porosity n_0 was estimated from the effective minus-cement porosity having been corrected for the carbonate content of the host sediment and the volume of the septarian cracks. The determined initial porosity was compared with empirical pore volume and compressibility data of modern sediments (Wetzel, 1990; Al-Khafaji *et al.*, 1992; Hong *et al.*, 2020). This equation applies for ‘pure’ mechanical compaction that very likely affected the host

sediment during the early stages of concretion formation. The equation is compatible with ‘classical’ compaction curves as established, for instance by Athy (1930), for the upper few hundreds of metres of burial (Bayer & Wetzel, 1989). The burial history of the radish concretions was evaluated by applying geohistory analysis (van Hinte, 1978; Wangen, 2010) and using the time scale of Hardenbol *et al.* (1998). Sediment thickness was restored by using the sedimentation–compression diagram (see above) for the five stratigraphic intervals above the concretions.

RESULTS

Occurrence, shape and size

On average, one radish concretion was found within a bed surface area of about 25 m^2 . The long axis of a concretion is oriented nearly perpendicular to bedding (Fig. 3). The host sediment is deformed around a concretion; the interval bent around the lower part is about two times thicker than that around the upper part. Undeformed horizontal laminae may pass from the host sediment into the concretion roughly between the upper third and the middle third; an interval where many radish concretions reach their maximum diameter and exhibit laminae rich in silt and fine sand (Fig. 4). The host sediment contains $3.0 \pm 0.2\%$ micritic carbonate and 0.8 to 2.7% organic carbon. The carbonate content below, above, beside and at about 10 to 20 cm distance from the concretions does not vary considerably. In the completely disintegrated, remoulded host sediment, shrinkage cracks formed if the water content dropped below 32 to 34% relative to the dry weight of the sample (= $47 \pm 1\%$ porosity; void ratio $e = 0.88$).

The radish concretions have a nearly circular cross-section, and their overall geometry varies from columnar to inverted pear-shaped (stipe-downward). The concretions measure up to 19 cm in length and 12 cm in diameter. The smallest specimen is 5 cm high and 4 cm wide. On average they are 11.5 cm high and 6.5 cm wide (Table 1). In one case, two concretions have grown laterally together (Fig. 4). Geometrically, the concretions comprise three parts: (i) an upper obtuse cone; (ii) a roughly cylindrical middle part that commonly exhibits the largest diameter; and (iii) a lower part resembling a downward acute cone (Fig. 4). Despite their variability in shape and size, both the upper and the lower tip of the concretions

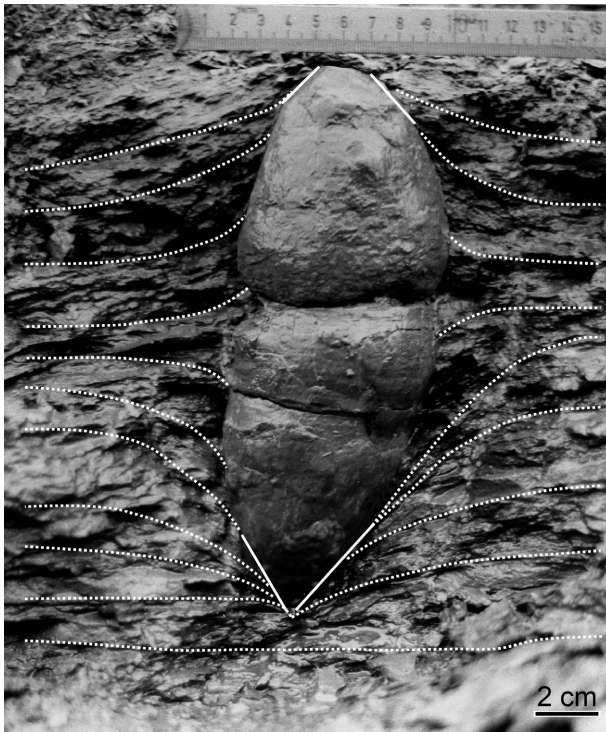


Fig. 3. An excavated radish concretion in place (photographed in 1981); around the concretion, sedimentary laminae were deformed (marked with white stippled lines) and shear planes developed along the lower and upper tip (marked by white lines).

show a rather uniform angle of aperture, $115 \pm 5^\circ$ and $65 \pm 5^\circ$, respectively (Table 1; Fig. 4).

In the upper part, the concretion surface is rather smooth. Within the interval of largest diameter, some remnants of sedimentary lamination can be present. The surface of the lower part exhibits some upward ramp-step structures as well as vertically oriented striations (Fig. 5). These are subparallel to each other and do not cross-cut. Pyrite can occur at the upper terminations of the striations (Fig. 5).

Internal structures

In longitudinal section, the concretions display three macroscopically different features: (i) an

axial part rich in pyrite; (ii) the concretion body; and (iii) septarian cracks cutting through both the body and axial part (Figs 6 and 7). The formation of septarian cracks marks the transition between ‘early diagenetic’ processes and ‘late diagenetic’ processes as categorized below. This terminology is used throughout the following sections.

Axial part

Two features are observed in the axial part:

1 An irregular, but nonetheless nearly vertical pyrite-rich axis traverses the whole concretion in the centre and crops out at its upper and lower tip.

2 Following along sedimentary laminae, zones of disseminated to pervasive authigenic pyrite extend outwards from the central axis at varying distances.

In coarse-grained layers pyritization extends farther outward than in fine-grained material (Fig. 4). There is no sharp boundary between the pyrite-rich axis and the laterally dispersed pyrite. Pyrite occurs in the axial part as massive mineralization with rare siliciclastic inclusions.

Concretion body

Material in the body of the concretion is dark greyish in colour, and accentuated by faint, dark-brown millimetre-thick, silt to fine-grained sand laminae. Within the upper part of the concretions, the laminae are slightly inclined downward towards the margin of a concretion, in the middle, commonly widest part, they are nearly horizontal, and in the lower part, they become increasingly inclined downward towards the centre, reaching the maximum dip at the lower tip of the concretion (Fig. 4). The middle part of a concretion characterized by undeformed horizontal laminae is called parent domain. Some intervals appear uniform, probably mixed by burrowers producing indistinct biodeformational structures that occasionally were overprinted by preferentially horizontal, tubular traces <1 cm in size.

Table 1. Geometrical measurements of 30 radish concretions

	Height of upper part h_1 [cm]	Length of middle part h_2 [cm]	Length of lower part h_3 [cm]	Total length [cm]	Maximum diameter [cm]	Angle at upper tip	Angle at lower tip
Mean	4.6	1.1	9.5	11.5	6.5	116°	63°
Minimum	1.9	0.0	3.7	5.0	4.0	110°	60°
Maximum	5.6	4.7	13.6	19.0	12.0	120°	70°

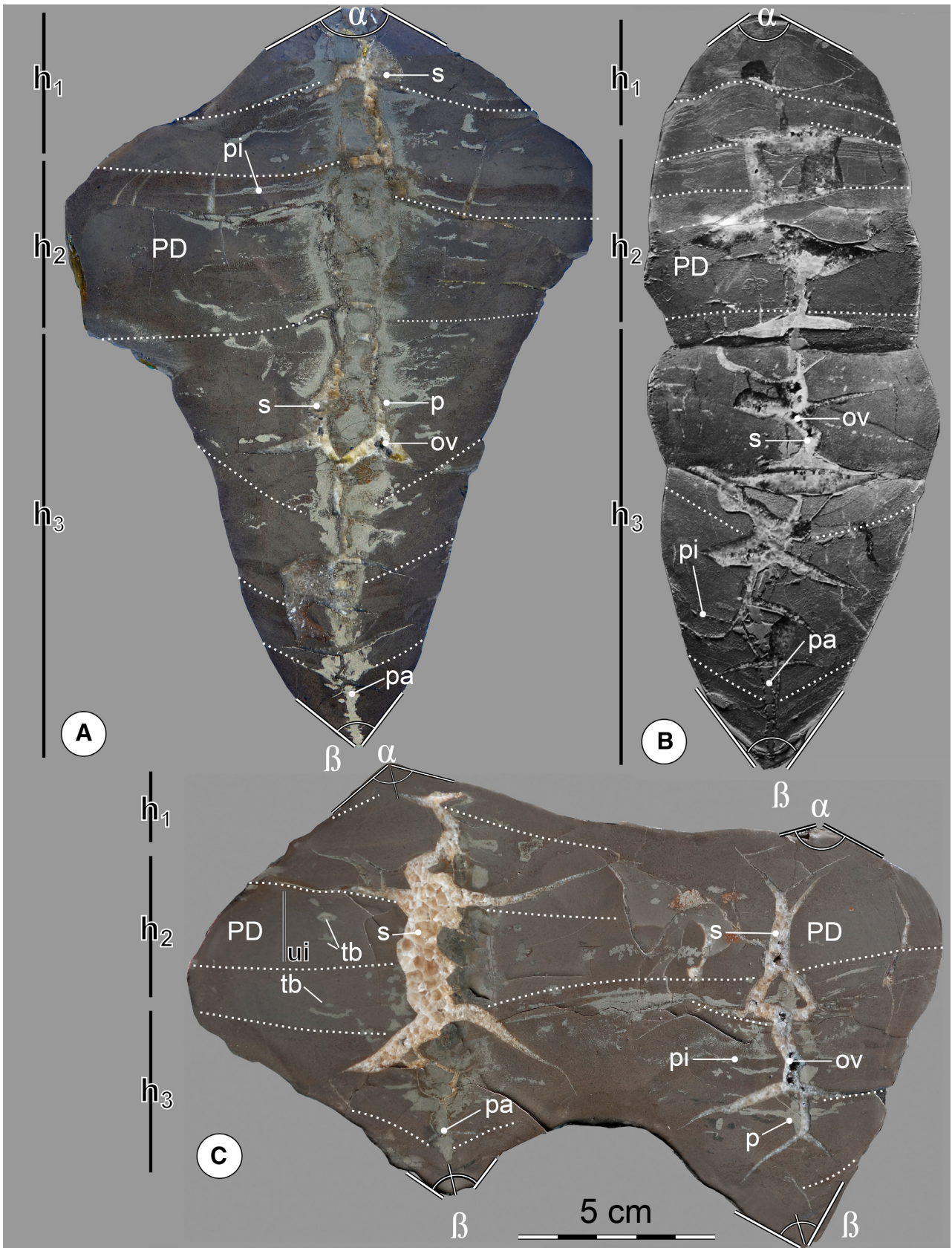


Fig. 4. Radish concretions display shapes varying from pear-shaped (A), columnar (B) to coalesced (C). Internal structures suggest concretion growth during compaction as indicated by lamination becoming increasingly inclined towards the tips of the concretions (marked by white stippled lines). Undeformed nearly horizontal laminae characterize the part that was cemented first (PD = parent domain having the height h_2). The upper and the lower domains grown during compaction have heights h_1 and h_3 (see Table 1). Concretions formed around an axial part consisting of pyrite (p) comprising a central pyrite axis (pa) and lateral pyrite impregnations (pi). All structures are cross-cut by septarian cracks filled with white calcite spar (s) but may also exhibit some open voids (ov); locally uniform intervals (ui) homogenized by burrowing organisms and tubular burrows (tb) occur. Typical angles of aperture at the top (α) and at the base (β) characterize sediment behaviour during compaction and concretion growth (Table 1).

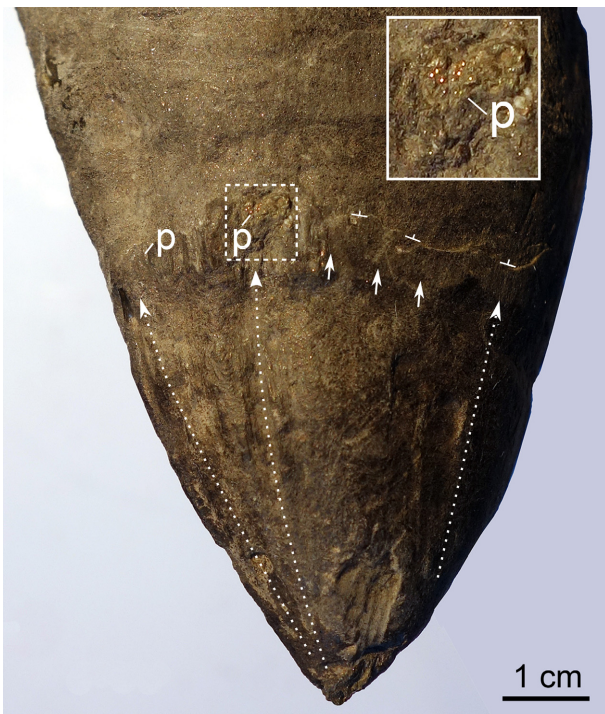


Fig. 5. Striations (white stippled lines) on the surface of the lower part of a radish concretion document differential compaction and sediment failure and pyrite crystals (p) appear to have sculpted the surface (for details see text); framed area by broken line is shown in the inset; at the end of striations, ramp (white arrows) and down stepping (\perp) structures may be present.

The concretions appear to be fully cemented and contain up to 87% CaCO_3 ; the remainder are siliciclastics and pyrite but they have not lost the potential to shrink since subtle fissures opened after they had been stored for about 40 years in a dry environment at room temperature, as documented by a picture of a transverse section taken 1982 and published a few years later (Wetzel, 1992, fig. 1). The

hairline to approximately 1 mm wide cracks originate on the surface and narrow inward (Fig. 6) and are thus distinct from (and locally cut) the outward-tapering, cemented, septarian cracks.

The cement is micritic and contains small pyrite grains rarely exceeding 20 μm in size (Fig. 8A and B). They are usually anhedral and massive and do not show a grape-like structure. Although rare, true framboidal grains occur as well. Microscopic analyses do not provide any evidence for displacive growth of the authigenic carbonate minerals such as grain-enveloping rims or radial fibrous calcite cements (e.g. McBride *et al.*, 2003). Within the concretion body no detrital carbonate grains could be identified and the calcite displays a micritic texture. The calcite comprising the concretion body shows an overall moderate orange cathodoluminescence colour with up to 10 to 15% tiny brighter yellow and dark brown calcite grains dispersed throughout (Figs 8D and 9C).

Septarian crack fill

Cemented septarian cracks are present in all studied concretions and cut through both the pyrite-rich axial part and the surrounding concretion body. They are widest in the concretion centre, and taper outward to become very narrow and disappear before reaching the concretion surface. Some septarian cracks appear to follow silt and fine sand-bearing laminae whereas others are curved and tend to orient either parallel or perpendicular to the concretion surface. Opposite surfaces bounding wide septarian cracks do not exactly match (Fig. 6). For five concretions, the volume of the septarian cracks was quantified as being $9.8 \pm 3.2\%$. Geometrically, the septarian cracks are very similar to those formed within the host sediment during shrinkage experiments (Fig. 7).

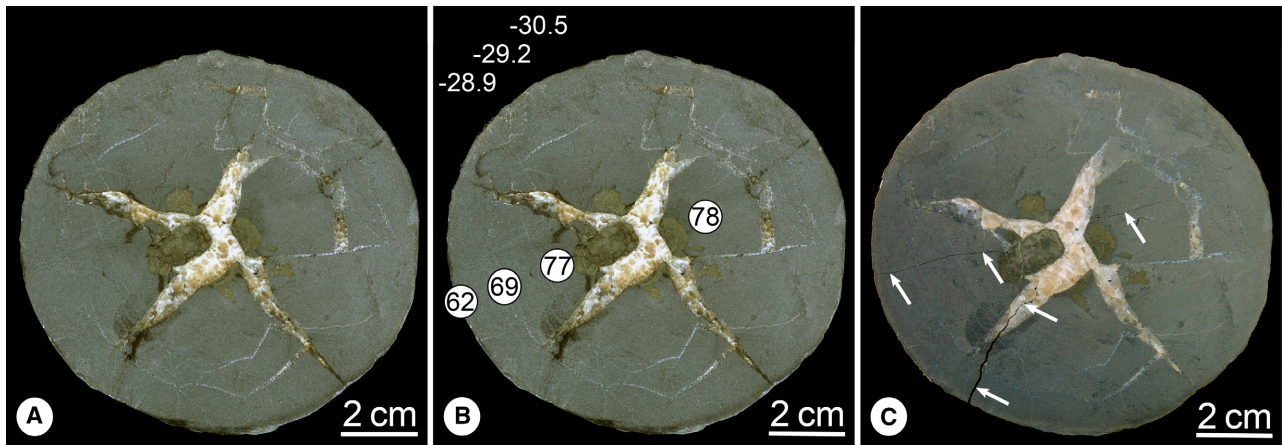


Fig. 6. Cross-section of a radish concretion with newly formed cracks. (A) Freshly cut concretion (picture taken in 1982). (B) Same picture as (A), carbonate-cement content (black encircled numbers; published by Wetzel, 1992, fig. 1) and $\delta^{13}\text{C}$ values of the same samples given in ‰ (white negative numbers). (C) Same sample as in (A) and (B) after long-term (*ca* 40 years) storage under dry conditions with newly formed shrinkage cracks marked by white arrows.

Macroscopically, the septarian cracks are filled with millimetre-sized, blocky, clear to translucent whitish calcite crystals. Occasionally, the central part of a septarian crack contains an open void (Fig. 4). Two generations of septarian cracks and their infill are distinguished petrographically. The first crack generation (sc-1) commonly has a thin, macroscopically visible lining of pyrite crystals (<0.2 mm large) that exhibit subhedral to euhedral morphology seen at high magnification and/or is filled with calcite-1 (sc-1/1) forming an up to 0.2 mm thick lining having acute crystal terminations towards the centre of the cracks and showing a moderately bright orange to yellow cathodoluminescence colour similar to that of the concretion body (Figs 8D and 9). The second generation of septarian cracks (sc-2) is not

lined with pyrite (Figs 8B to D and 9) and exhibits a fill with equant calcite-2 spar (<1.5 mm large; sc-2/2) that occasionally occurs in the central part of the first-generation cracks (sc-1/2) and has a dull brown cathodoluminescence colour (Figs 8D and 9).

Geochemical data

The carbonate content of the concretion body varies depending on sediment grain-size and position within the concretion (Table 2; Fig. 10). The parent domain has the highest carbonate content of *ca* 80%. Towards the margins, the carbonate content decreases, particularly within the lower cone-shaped concretion part to below 70%, reaching a minimum of *ca* 55% at the

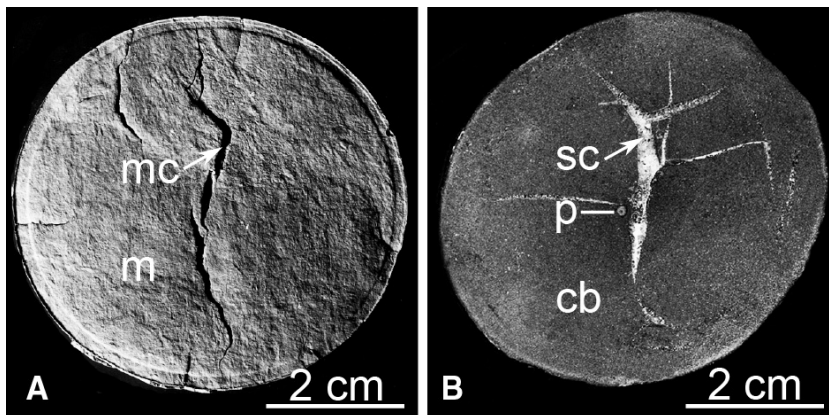


Fig. 7. Mud cracks and septarian cracks. (A) Mud cracks (mc) formed during tests to determine the shrinkage limit of the host sediment (m); note widening of crack inward. (B) Cross-section of a radish concretion displaying similar arrangement of septarian cracks (sc) as shown in (A); cb = concretion body, p = pyrite constituting the axial part of the concretion.

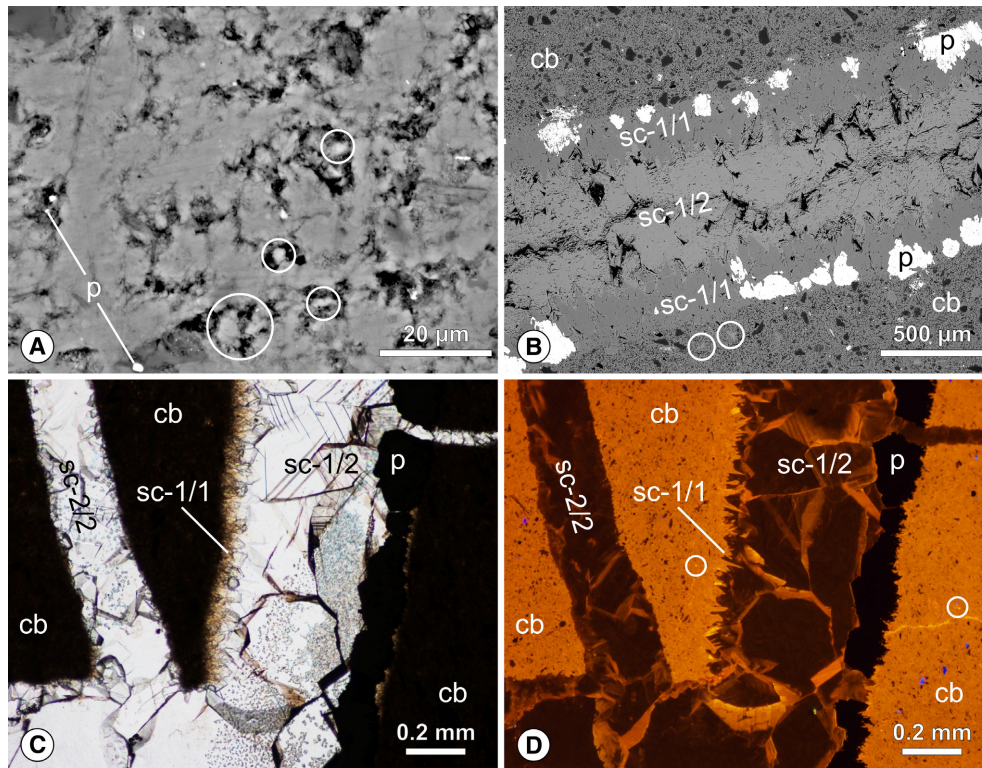


Fig. 8. Differences in texture and elemental composition between different generations of calcite cement. (A) and (B) Concretion body (cb) is predominantly composed of low-Mg micritic calcite with dark grey colour in BSE images, but also slightly brighter crystals with increased Fe content (white circles). Pyrite (p) occurs as small grains in the concretion body and as large subhedral to euhedral crystals lining the walls of the first generation septarian cracks (sc-1); calcite-1 cement in the first-generation septarian cracks (sc-1/1) exhibits analogous elemental composition and BSE image contrast to the dominant calcite in the concretion body, whereas the calcite-2 filling the second generation of septarian cracks (sc-1/2) exhibits increased Fe content and is brighter in the BSE image (B). (C) and (D) Paired photomicrographs [plane parallel transmitted light in (C) and cathodoluminescence image in (D)] of two generations of septarian crack fill; the first one (sc-1) is lined with pyrite and calcite-1 (sc-1/1; moderate orange and brighter yellow cathodoluminescence colour) followed by calcite-2 (sc-1/2; dull brown cathodoluminescence colour) whereas the second crack generation (sc-2) is filled only with calcite-2 (sc-2/2). The calcite-1 (sc-1/1) exhibits mostly the same cathodoluminescence colour as in the concretion's body; additionally calcite with the distinctive brighter yellow cathodoluminescence colour occurs both in the early septarian calcite (sc-1/1) and in the concretion body (encircled). Note that the generally dull brown luminescent late septarian calcite contains apparent brighter luminescence along crystal boundaries and cleavage cracks, which indicates that this is an edge effect.

lower tip (Fig. 10). Considering the rather uniform carbonate content ($3.0 \pm 0.2\%$) of the host sediment close to and at 10 to 20 cm distance from the concretions, and the effects of volume change due to septarian crack formation, the effective minus-cement porosity in the parent domain is *ca* 75%, and decreases to *ca* 60% at the upper tip and to *ca* 50% at the lower tip. The non-carbonate phase consists of siliciclastic clay, silt, minor fine-grained sand and pyrite.

The concretion body is cemented by low-Mg calcite containing 1.4 to 4.4 mol% MgCO_3 . In the cement of some concretion bodies, disseminated crystals of FeCO_3 increase to 1 mol%, and

show a brighter grey colour in back-scattered electron images (BSE; Fig. 8A and B). The first-generation septarian calcite exhibits similar or slightly higher MgCO_3 content (<6 mol%), whereas FeCO_3 is usually below detection limit. Similar elemental composition of concretionary and first-generation septarian cements is also reflected in their similar BSE intensity and cathodoluminescence colours (Fig. 8B to D). The second-generation septarian, blocky calcite contains less MgCO_3 (<1 mol%), whereas its FeCO_3 content increases to 1 to 3 mol%, with a corresponding brighter intensity in BSE images (Fig. 8B). The elevated FeCO_3 content is

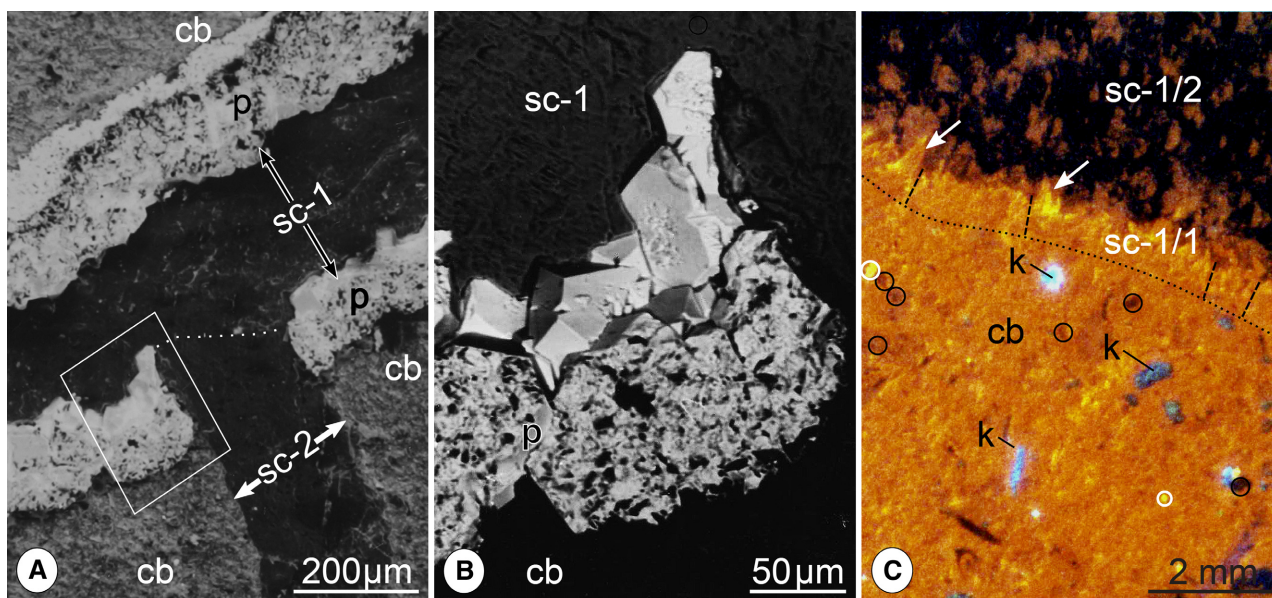


Fig. 9. Two types of calcite-filled septarian cracks formed within radish concretion bodies (cb). (A) and (B) Back-scattered electron images of both crack types. (A) first generation (sc-1) is lined by pyrite (p) and the second generation (sc-2) is not; white frame marks detail shown in (B). Note the euhedral crystal morphology of pyrite in (B). (C) Cathodoluminescence photomicrograph of concretion body (cb) containing K-feldspar (white-blue, k), traversed by the first generation septarian crack. Along the crack surface (stippled black line), luminescent euhedral crystals of calcite-1 (white arrows; sc-1/1) grew approximately perpendicular to the crack wall (black broken line). The crack fill is blocky calcite-2 with a dull brown cathodoluminescence colour (sc-1/2) indicating elevated Fe-content. Calcite displaying the same cathodoluminescence colours to those represented by both septarian calcite generations are also present in the concretion body, bright yellow (white encircled) and dull brown (black encircled).

responsible for the dull luminescence of this calcite (Fig. 8C and D) due to the quenching effect of Fe^{2+} in calcite (Machel, 1985).

The C and O isotope composition of bulk samples from five concretions was measured (Table 2; Fig. 11). All concretions show similar isotopic values; $\delta^{13}\text{C}$ ranges from -36.1 to -29.6‰ (average -32.6‰) and $\delta^{18}\text{O}$ from -3.0 to -0.4‰ (average -2.1‰) for the concretion body ($n = 38$), whereas $\delta^{13}\text{C}$ ranges from -3.0 to -0.7‰ (average -1.3‰) and $\delta^{18}\text{O}$ from -10.9 to -10.4‰ (average -10.6‰ ; $n = 7$) for the late septarian crack fill. The parent domain exhibits the lowest $\delta^{13}\text{C}$ values but does not show a radial centre-to-edge trend (Fig. 10) although $\delta^{13}\text{C}$ values increase from the parent domain upward and downward towards the concretion tips (-36 to -31‰ ; Fig. 10). Furthermore, the $\delta^{13}\text{C}$ values tend to increase with decreasing carbonate content ($r = -0.50$; Fig. 12). Oxygen and carbon isotope data also follow a pronounced negative covariant trend exhibiting a rather high correlation coefficient $r = -0.66$. The host sediment carbonate has average isotope values of $\delta^{13}\text{C} -2.5 \pm 0.4\text{‰}$ and $\delta^{18}\text{O} -3.6 \pm 0.4\text{‰}$ ($n = 4$; Fig. 11).

INTERPRETATION AND DISCUSSION

The concretions occur within a sediment succession that experienced recurrent reworking and discontinuous deposition and, thus, represented a period of low sediment net-aggradation (Franz & Nitsch, 2009; Geyer & Gwinner, 2011). This situation matches the scenario that mud-hosted concretions commonly need to reside for several hundreds to a few thousands of years within a geochemical zone favourable for their growth (e.g. Raiswell & Fisher, 2004). The radish concretions developed under rather stable geochemical conditions within the sulphate reduction zone because pyrite and carbonate co-occur and are adjacent to each other; pyrite constitutes the vertical axis in the centre and is also finely dispersed within the surrounding calcite-cemented concretion body.

Geochemical data

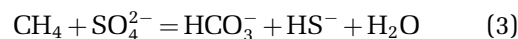
The $\delta^{13}\text{C}$ values ranging from -36 to -30‰ , as well as the co-occurrence of pyrite and authigenic carbonate, indicate that the alkalinity providing carbonate cement originated in the sulphate

Table 2. Geochemical data of radish concretion bulk samples

No.	Sample*	$\delta^{18}\text{O}$ [‰]	$\delta^{13}\text{C}$ [‰]	Carbonate content [%]	MgCO_3 [%mol]
116	pd	-1.6	-35.2	78.0	
117	cb	-2.0	-31.8	66.4	3.9
118	pd	-1.8	-32.9	76.5	3.7
119	pd	-1.6	-33.8	78.2	4.3
120	cb	-1.7	-33.7	68.0	3.6
121	cb	-2.5	-30.9	66.5	3.9
122	cb	-2.1	-32.2	68.8	4.4
123	cb	-2.4	-31.0	61.9	3.8
124	cb	-2.0	32.8	54.9	3.6
125	pd	-0.4	-32.0	–	–
126	pd	-1.3	-35.7	–	–
127	pd	-0.8	-34.4	78.0	–
131	sc	-10.5	-0.7	100.0	–
132	sc	-10.8	-1.1	100.0	–
133	sc	-10.5	-0.8	100.0	–
301	cb	-2.5	-32.7	79.8	–
302	cb	-2.1	-33.5	80.5	–
303	cb	-3.0	-30.3	82.3	–
304	pd	-1.6	-35.9	86.7	–
305	pd	-1.5	-36.1	85.7	–
306	pd	-1.6	-34.9	85.8	–
500	pd	-2.4	-32.4	82.2	–
501	pd	-2.0	-32.9	85.7	–
502	pd	-2.2	-32.9	84.4	–
503	cb	-2.1	-33.6	85.6	–
504	cb	-2.4	-31.8	71.4	–
505	cb	-2.5	-31.7	82.7	–
506	cb	-2.9	-30.1	77.1	–
701	hs	-3.6	-2.8	3.1	1.5
702	hs	-3.1	-2.3	2.8	1.0
703	hs	-3.9	-2.9	2.9	1.0
704	hs	-3.8	-2.1	3.2	1.4
711	sc	-10.4	-3.0	100.0	1.4
712	sc	-10.9	-0.7	100.0	1.3
721	cb	-2.3	-30.5	68.0	3.2
722	cb	-2.1	-32.5	77.8	3.1
723	cb	-2.9	-29.6	62.1	3.6
724	cb	-2.0	-31.0	77.8	3.4
725	cb	-2.1	-32.6	76.4	–
726	cb	-2.1	-31.6	76.0	3.7
727	cb	-2.1	-32.5	74.6	3.8
728	cb	-2.3	-32.2	74.9	3.6
729	cb	-2.4	-31.6	69.2	3.4
901	pd	-1.8	-32.3	–	–
903	cb	-2.2	-32.9	–	–
904	cb	-2.6	-31.6	–	–
905	cb	-2.2	-32.9	–	–
906	sc	-10.4	-2.0	–	–
907	sc	-10.7	-0.9	–	–

* cb = concretion body; hs = host sediment; pd = parent domain; sc = septarian crack fill.

reduction zone where organic compounds became oxidized (e.g. Irwin *et al.*, 1977; Whiticar, 1999; Hudson *et al.*, 2001). Two gross-reactions for the anaerobic oxidation of organoclastic material (OSR; Eq. 2) and the anaerobic oxidation of methane (AOM; Eq. 3) are responsible for generating alkalinity and sulphide, which simultaneously fostered the concomitant precipitation of carbonate and Fe-sulphide (e.g. Burdige, 2006):



The isotope data measured for the different concretions match the same trend (Fig. 11). The datapoints on the isotope plot are parallel to the line modelled by Bojanowski (2012, fig. 9) for mixing between two bicarbonate sources, namely OSR and AOM characterized by distinctively different isotope signatures. Besides pronounced fractionation of carbon isotopes (e.g. Irwin *et al.*, 1977; Burdige, 2006), OSR may also lead to oxygen isotope fractionation (e.g. Sass *et al.*, 1991; Thaler *et al.*, 2020). These microbially mediated reactions take place within the sulphate–methane transition zone (Claypool & Kaplan, 1974; Barnes & Goldberg, 1976). The positive correlation between $\delta^{13}\text{C}$ and $\delta^{18}\text{O}$ suggests the mixing of two different sources of bicarbonate (Snyder *et al.*, 2007; Mavromatis *et al.*, 2014). Although the isotope composition of the concretion body could be explained by mixing of AOM-derived and late diagenetic bicarbonate, the latter having datapoints on the isotope plot roughly along the trend line for concretion bodies (Fig. 11); in organic-rich mud, OSR is a ubiquitous process (e.g. Burdige, 2006; Raiswell & Canfield, 2012) and, hence, has to be taken into account. It is important to note that the depositional and palaeoceanographic conditions in the basin examined were different from those in Central Paratethys (e.g. Bojanowski *et al.*, 2018) where the rocks investigated by Bojanowski (2012) were deposited. So it is not possible to directly apply the isotope composition of the OSR and AOM endmembers from Bojanowski's model (Bojanowski, 2012) to this work. However, the striking similarity of the isotope trend of the radish concretions to that modelled by Bojanowski (2012) indicates that their isotope

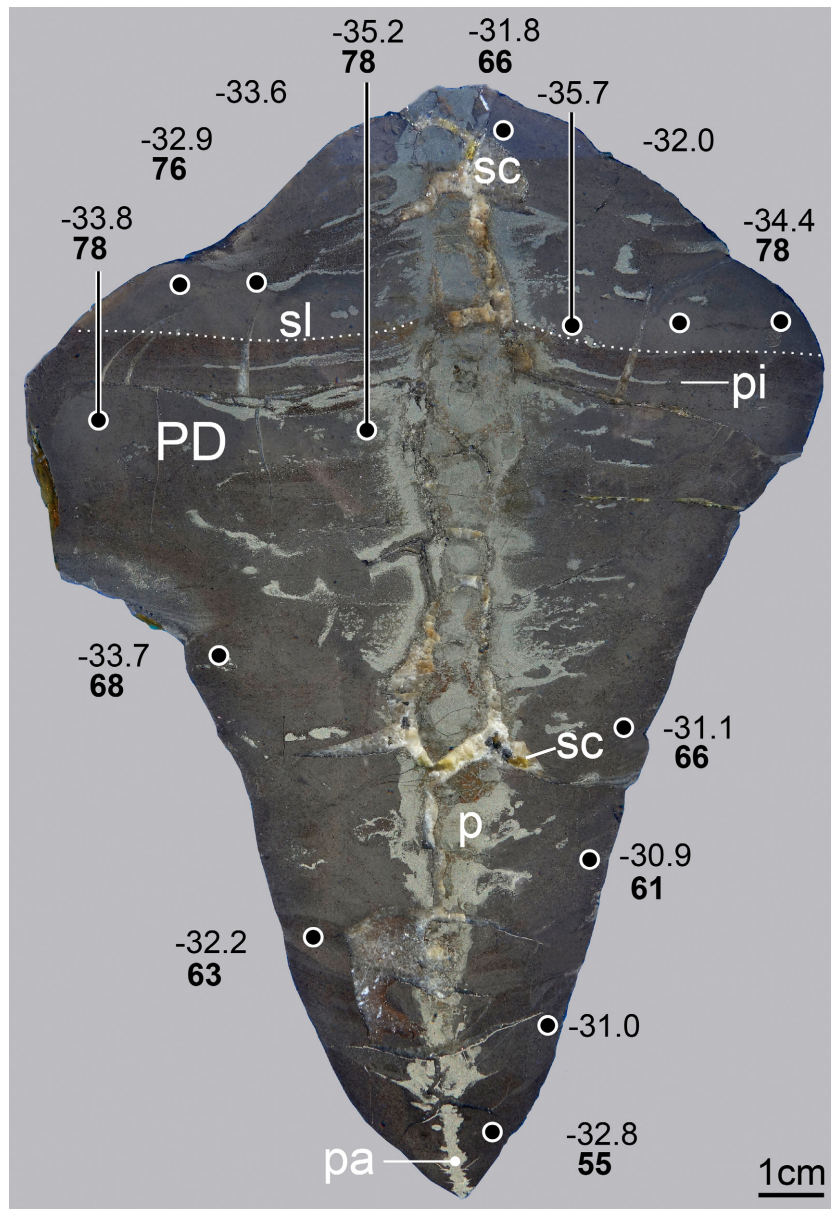


Fig. 10. Variability of bulk carbon isotope values (negative numbers) and carbonate content (bold numbers) along a longitudinal central section of a radish concretion; the parent domain (PD) of the concretion is characterized by undeformed sediment laminae (sl); carbonate content decreases away from the parent domain while the carbon isotope values increase. Away from the central pyrite axis (p, pa), pyrite cemented (pi) the concretion body preferentially along laminae, septarian cracks (sc) cross-cut the central pyrite-rich part as well as the concretion body. Black dots indicate where concretion was analyzed.

composition was chiefly controlled by mixing between these two bicarbonate sources, namely OSR and AOM. Furthermore, a marine bicarbonate component contributed a rather constant and considerable amount, supposedly 10 to 30%, to the cement as implied by the tight covariation of oxygen and carbon isotope values.

The rather uniform $\delta^{13}\text{C}$ values around -35% within the parent domain imply rapid, pervasive cementation (e.g. Raiswell & Fisher, 2000). At a later stage, when the concretions grew upward and downward, the carbon isotopes became slightly heavier with values of $\delta^{13}\text{C}$ about -30% . This $\delta^{13}\text{C}$ shift to higher values could be

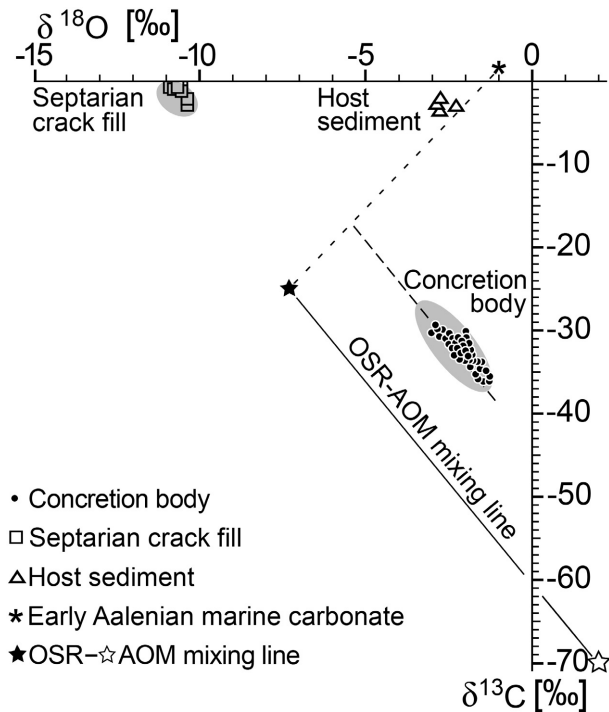


Fig. 11. Bulk carbon and oxygen isotope values of several radish concretions, host sediment and reference line indicating the mixture of bicarbonate produced within the sulphate reduction zone by anaerobic oxidation of organoclastic material (OSR) and methane (AOM) at varying proportions (for details see Bojanowski, 2012). The trend of the isotope data of the concretion body ($r = -0.66$) is parallel to the OSR-AOM trend (solid line) but shows a shift (marked by broken line) towards early Aalenian marine carbonate (marked by asterisk representing a simplified mean value as seawater composition varies for $\delta^{18}\text{O} = -1 \pm 0.5\text{‰}$ and $\delta^{13}\text{C} = +1.5 \pm 1.5\text{‰}$; for details see text).

explained by several processes, such as a preferential supply of isotopically heavier methane since ^{12}C is more rapidly consumed due to the kinetic isotope effect associated with AOM (e.g. Whiticar, 1999) or an increasing proportion of alkalinity provided by fermentation during methanogenesis or by OSR (e.g. Whiticar, 1999; Wheeler & Stadnitskaia, 2011). The latter seems more probable, because sulphate reduction operated during the precipitation of the early septarian calcite, attested by the association with euhedral pyrite, which is presumably coeval to the late generation of microcrystalline calcite in the concretion body. Yet, the increase of $\delta^{13}\text{C}$ values is associated with concomitant decrease of carbonate content in the upper and lower

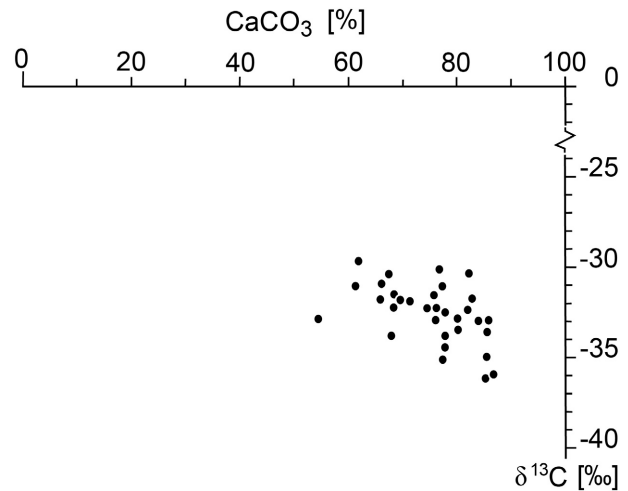


Fig. 12. Carbonate content versus $\delta^{13}\text{C}$ values of the concretion-body cement showing some covariation (correlation coefficient -0.50 ; for details see text).

domain (Figs 10 and 12), which allows another interpretation. The C isotope outward trend may simply reflect the outward increasing ratio between detrital and authigenic carbonate due to increasing compaction during concretionary outward growth.

Internal structure and geotechnical aspects

The sparse bioturbational structures preserved within the concretions are typical of a low-oxygenated depositional environment, which are commonly produced by organisms living at a shallow depth below the sediment surface (e.g. Wetzel *et al.*, 2011; Campetella *et al.*, 2020). Inclined laminae within the concretions document their growth in compacting mud. Cementation started around a nearly vertical, Fe-sulphide enriched axis in the parent domain because the sedimentary laminae are \pm horizontal and undeformed and the minus-cement porosity is highest (75 to 80%). Such high porosity values suggest an onset of concretion growth in a very shallow burial depth (<10 m; e.g. Baldwin & Butler, 1985; Dix & Mullins, 1987; Wetzel, 1990; Duck, 1995). The Fe-sulphide rich axis is interpreted to have been a dewatering tube that formed below the porous surface sediment layer, as observed in modern sediments (Fig. 13). It probably acted as a preferential migration pathway for both methane from below and sulphate from above as it crops out at both tips of a concretion. In modern sediments, such thin tubes occur at depths of

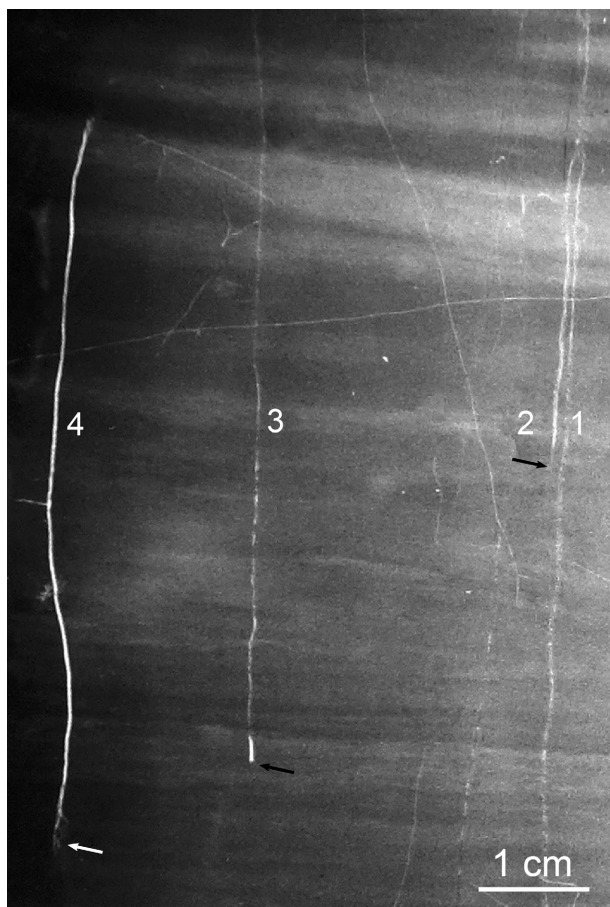


Fig. 13. Fe-sulphide lining within dewatering tubes in modern deep-sea mud (Sulu Sea; core 14224-1, 154 to 161 cm below sediment surface; for location see Wetzel, 1983; X-ray radiograph negative; mud – dark, Fe-sulphides – light). Numbers refer to different stages of development; Fe-sulphide precipitation along dewatering tubes being diffuse (1, 2), discontinuous (3) and massive (4); the lower tips of the tubes (marked with white and black arrows) being diffuse (1, 2), sharp (3) or diffuse funnel-like (4). Two tubes may form adjacent to each other (1, 2). Around the Fe-sulphide tubes no carbonate cementation is evident that would result in higher X-ray attenuation and, hence, lighter tone; therefore, the Fe-sulphides likely precipitated in the upper part of the sulphate reduction zone.

1 m or less, and are interpreted to represent dewatering structures or small burrows, such as *Trichichnus* (Fig. 13; Wetzel, 1981, 1983, fig. 3; Löwemark, 2003). Both tube types can reach a length of >1 m (Wetzel, 1981; Weaver & Schultheiss, 1983).

The permeability of the host sediment affected the growth of the concretions, in particular during the initial phase. In the parent domain, the

largest diameter of the radish concretions coincides with silty to fine-grained sandy layers that had an enhanced permeability because of the coarser grain size when compared to the mud above and below (e.g. Mitchell, 1993). Such layers become preferentially cemented (e.g. Einsele & Kelts, 1982; James, 1985). Seawater carrying sulphate and Ca^{2+} was supplied by diffusion or via the central tube while methane migrated upward from below into the more permeable layers. AOM and OSR produced oversaturation of (bi)carbonate that precipitated around the tube and within the more permeable layers, and led to formation of the parent domain. In contrast, tubular radish concretions not exhibiting an enlarged diameter of the parent domain do not contain layers considerably enriched in coarse silt or fine sand.

After initial cementation, the parent domain was evidently resistant against compaction and did not deform any longer (Fig. 4). In contrast, the sediment above and below the parent domain was affected by differential compaction during further burial as recorded by the increasing inclination of the laminae and the concomitant decrease in minus-cement porosity towards the tips of the concretions (Fig. 10). As methane kept seeping upward and calcite precipitation continued below and above the parent domain, the layers already deformed by compaction became part of the concretions. The prevailing downward growth of the concretions implies that methane migrated upward by diffusion or by advection of pore water expelled during compaction (see Einsele, 1977). In addition, the upstreaming pore water might have provided (bi)carbonate. Evidently, not all upward-migrating methane and (bi)carbonate was consumed at the base of a concretion and moved further up to cement the upper domain. These processes added successive increments to the base and the top of the concretions and may have invoked fluid mixing during increasing compaction until pyrite clogged the tube and/or compaction significantly reduced mud permeability. Then concretion growth ceased because methane could no longer react with sulphate at the concretion sites.

Both deformed laminae within the concretions and striations on their surfaces record part of their formation history. The striations were formed by pyrite after the concretions' growth had ceased but the mud was still being compacted (see below). These features indicate differential movement between the host sediment and the concretions. The deformed laminae at the

base and the top of the concretions exhibit rather uniform angles of inclination and can be interpreted in terms of earth pressure theory that addresses the interaction between soil and man-made construction features such as walls and foundations. If a soil/sediment volume initially under at-rest stress condition is allowed to yield by compression in a vertical direction while spreading laterally, then the horizontal earth pressure coefficient decreases until it reaches a failure condition. The same is true for horizontal compression causing vertical displacement of soil/sediment. The two failure conditions are termed active and passive earth pressure, respectively (Mitchell, 1993). In case of the studied concretions within compacting mud, the lower part of the concretion is pressed relatively downward while the mud is displaced somewhat outward and, thus, matches the case of active earth pressure as indicated by the striations on the concretion's surface which document failure conditions in a geomechanical sense. In contrast, the mud above the top of the concretion moved relatively downward and, thus, matches the case of passive earth pressure. First, sediment laminae around the concretion deformed and finally the failure planes accentuated by the striations on the concretion surface developed (Fig. 5). The inclination of the planes reflects the properties of the host sediment including the critical angle of failure (θ). At the top of a concretion, the slip plane inclination is related to the passive earth pressure (θ_p) given by the formula:

$$\theta_p = 45^\circ - \varphi/2 \quad (4)$$

with φ as angle of internal friction of the sediment (e.g. Mitchell, 1993). At the base, the inclination of the slip plane is related to active earth pressure (θ_a) given by:

$$\theta_a = 45^\circ + \varphi/2 \quad (5)$$

The half angle of aperture at top (α) and base (β) of the concretions was used to calculate the angle of friction (φ) of the sediment during the final phase of concretion formation; $\varphi = 28 \pm 2^\circ$ (Table 1; Fig. 4). This value matches quite well φ data determined for silt-rich mud to muddy fine sand of $27 \pm 5^\circ$ (geotechdata, 2013). The relatively small variation of the angles at the base and top of the 30 concretions measured supports the application of earth pressure theory. As an analogue, the deformation phenomena around a growing radish concretion match the soil

mechanical considerations for a solid body such as a pipe embedded in soft material (e.g. Voellmy, 1937; figs 58 and 59).

The effective minus-cement porosity values of the concretions in combination with geotechnical data of modern fine-grained marine sediments allow estimation of the depth in which the growth of the concretions started and ceased (Fig. 14). Given an initial porosity of 75 to 80% and an onset of concretion growth in 5 to 10 m depth, modern equivalents of the host sediments have a compression index of *ca* 1.4 (e.g. Wetzel, 1990; Al-Khafaji *et al.*, 1992; Hong *et al.*, 2020). Lastly, at the lowest effective minus-cement porosity of 50 to 55% concretion growth ceased, corresponding to *ca* 100 m burial depth. This value, however, is an extreme obtained for the lower tip of concretions that experienced differential compaction (see above). When considering the effective minus-cement porosity of the upper tip of the concretions that is little affected by differential compaction, as indicated by the only slightly inclined laminae, the minus-cement porosity is in the range of 60 to 65%, which corresponds to a burial depth of 40 to 60 m (Fig. 14). Evidently, during concretion growth, sulphate could diffuse or migrate downward to this depth that is still in the range observed in modern, slowly accumulating sediments (e.g. Loyd & Berelson, 2016).

A downward expansion of the sulphate reduction zone keeping pace with deposition is likely as suggested by: (1) geohistory analysis (Fig. 15); and (2) pyrite-induced striations on the concretions' surface. Both (1) and (2) are discussed below.

1 The deposits directly above the strata hosting the radish concretions are characterized by discontinuous slow accumulation, and recurrent reworking (e.g. Franz & Nitsch, 2009; Geyer & Gwinner, 2011; see above). These 20 to 25 m thick deposits (decompacted thickness of *ca* 45 to 55 m) accumulated within 2.5 Myr (upper part of the comptum Subzone to the base of the sowerbyi Zone). Therefore, the period favourable for concretion formation could have lasted for up to 2.5 Myr during which the net-aggradation of sediment was $<3 \text{ cm kyr}^{-1}$.

2 The pyrite creating striations on a concretion's surface was either already present within the sediment or it precipitated on the surface. In the latter case, Fe-sulphide precipitation occurred in the upper part of the sulphate reduction zone where acidity is buffered by carbonate dissolution (e.g. Canfield & Raiswell,

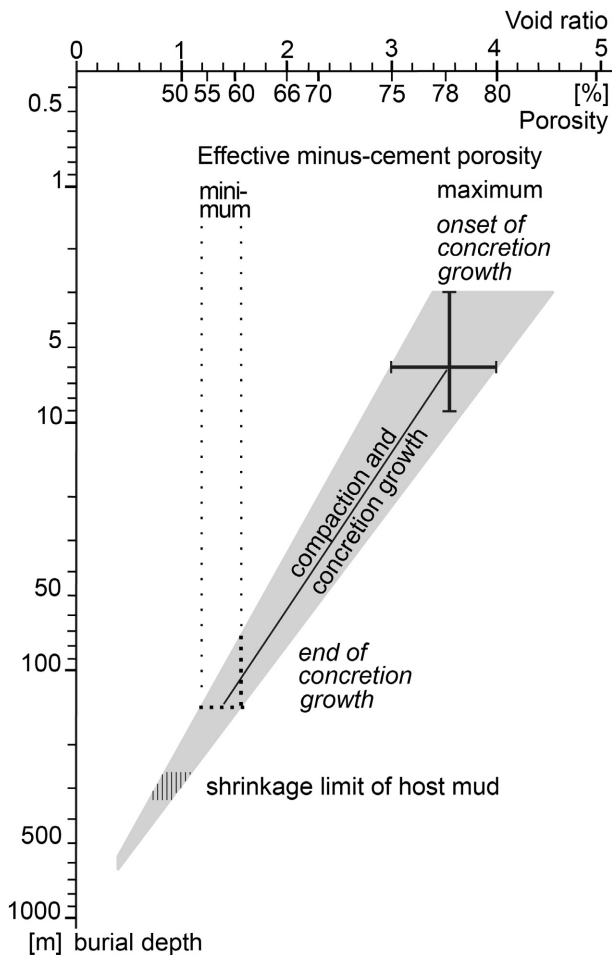


Fig. 14. Sedimentation–compression diagram [void ratio versus log(burial depth)] of a mud having a similar initial porosity as the host sediment of the radish concretions; the effective minus-cement porosity of the radish concretions (corrected for carbonate content of the host sediment and the septarian crack volume) provides information about onset (maximum) and termination (minimum) of concretion growth, occurring at ≤ 5 to 10 m and 60 to 100 m depth, respectively; value for shrinkage limit implies that septarian cracks might have formed at a greater depth (for details see text).

1991). If so, this pyrite indicates a downward expansion of the sulphate reduction zone after concretion growth has ceased but with further differential compaction occurring afterwards.

Septarian crack formation and fill by precipitation of ‘late’ cement

After AOM ceased, the microbial biomass related to AOM started to decay. The

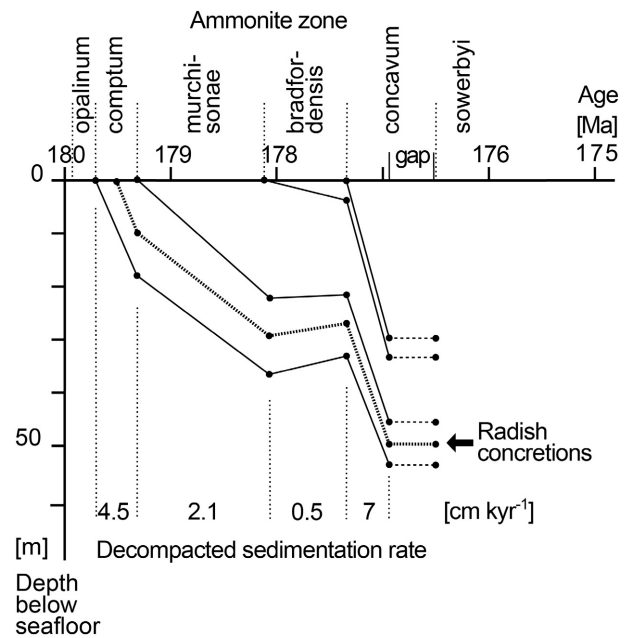


Fig. 15. Geohistory diagram (after van Hinte, 1978) showing the burial history of the interval containing the radish concretions using the initial sediment thicknesses; the decompaction factor was derived from the sedimentation–compression diagram (Fig. 14); similarly, compaction of the buried strata was calculated by the same method; time scale after Hardenbol *et al.* (1998). For each interval defined by an ammonite zone the uncompacted sedimentation rate was calculated.

degradation of microbial substances and the dehydration of organo-mineralic complexes might have caused septarian crack formation (e.g. Duck, 1995; Hendry *et al.*, 2006). Organic matter enhances plasticity of mud and its shrinkage limit (e.g. Mitchell, 1993; Izdebska-Mucha & Wójcik, 2013). Therefore, shrinkage cracks would form at a higher porosity (e.g. Izdebska-Mucha & Wójcik, 2013). Based on this finding, there is no reason that this is also not valid for the enrichment of a concretion’s interior by microbial substances. Therefore, the porosity data obtained by shrinkage experiments represent minimum values. Unfortunately, the role of microbial substances in septarian crack formation can hardly be quantified because its amount and composition is not known because it is already degraded (Hendry *et al.*, 2006). The outward narrowing shape of septarian cracks implies their formation in still plastic material (e.g. Wetzel, 1992; Hudson *et al.*, 2001; Loyd & Berelson, 2016). The mismatch of surfaces bounding opposite parts of a septarian crack

supports this deduction. In the cracks, both well-developed pyrite as well as rhombohedral calcite crystals started to grow and their idiomorphic morphology and large size are typical of slow growth in open voids (Fig. 9; Tucker & Wright, 1990).

The different fillings of the septarian cracks document a change in the geochemical composition of the pore fluid. The fill of the first-generation cracks started within the sulphate reduction zone where reactive Fe was also available as indicated by the pyrite lining the cracks. The euhedral nature of the pyrite suggests a low supply of Fe and/or sulphide (e.g. Taylor & Macquaker, 2000). In contrast, the fill of the second-generation of cracks does not show a Fe-sulphide lining, but is filled with blocky, dull-luminescent calcite with elevated Fe^{2+} content. This shows that reactive Fe was still available, but sulphate reduction no longer operated. The concretions apparently entered a diagenetic zone, where the calcite within the septarian cracks precipitated from completely different fluids, which resulted also in their higher Fe content, relatively heavy carbon ($\delta^{13}\text{C} \sim -1.5\text{‰}$) and light oxygen isotopes ($\delta^{18}\text{O} \sim -10.5\text{‰}$). This was probably a deep burial setting, where HCO_3^- was mobilized from carbonates in the surrounding rocks, as suggested by very similar $\delta^{13}\text{C}$ values for the septarian calcite and the detrital carbonate in the surrounding mudstone. The elevated burial temperature relative to the depth of concretion growth may explain the strong ^{18}O depletion in the septarian calcite (Bojanowski *et al.*, 2014). Based on the assumption that the pore fluid had a seawater composition, septarian fill calcite was precipitated at a temperature of 60 to 70°C. These values are rather close to the maximum temperature range that the upper part of the Opalinuston Formation experienced (75 to 85°C; Mazurek *et al.*, 2006; Elie & Mazurek, 2008). Therefore, precipitation of septarian crack fill during exhumation is much less likely, as flux of meteoric fluids typically leads to depletion of both ^{13}C and ^{18}O in bicarbonate (Swart, 2015), which is not observed here. Alkalinity was probably provided at a low rate as indicated by the large calcite crystal filling the cracks (e.g. Bathurst, 1975).

The formation of shrinkage cracks after the concretions were kept under dry conditions for about 40 years has implications for the interpretation of the bulk carbon and oxygen isotope data. Despite a high cement content of up to 83%, the concretions still contained open pores; otherwise the

shrinkage cracks could not form (e.g. Mitchell, 1993). Pervasive cementation, therefore, did not necessarily eliminate all porosity. Therefore, during late diagenesis after septarian crack formation, the ions constituting the septarian crack fill could diffuse or migrate within water films along grain boundaries or within micropores through the concretion body because the septarian cracks did not reach the concretion's surface. Thus, carbonate precipitated not only in the septarian cracks but also very likely in the still open pores within the concretion body as evidenced by the yellow and dull calcite crystals within both the septarian cracks and the concretion body (Figs 8 and 9).

The amount of late cement is hard to quantify because it is dispersed throughout the concretion body, but cathodoluminescence microscopic analyses and shrinkage experiments allow for a rough estimate. When the septarian cracks formed, the maximum value of the not-yet-filled pore volume is given by that obtained at the shrinkage limit of the host sediment, in the range of ca 47% porosity. This value is only an estimate because organic matter affects the plasticity of mud and the shrinkage limit of fine-grained sediments (e.g. Busch & Keller, 1981; Keller, 1982; Izdebska-Mucha & Wójcik, 2013). The minus-cement porosity of those parts of the concretions traversed by the outermost tip of the septarian cracks indicate that they started to form at a minus-cement porosity of 60% or less. This value is used for a simple volume calculation (Fig. 16). The minus-cement porosity of the parent domain is ca 80% (having $v_p : v_s = 4 : 1$ where v_p = volume of pores, v_s = volume of solids) that became filled by early cement until septarian cracks formed at 60% porosity ($v_p : v_s = 1.5 : 1$). If so, early cement filled 2.5 volume units and 1.5 volume units were still open; of that, 0.5 volume units were transformed into septarian cracks. Consequently, 1 volume unit within the concretion body was available for precipitation of late cement (Fig. 16).

To estimate the composition of the diagenetic fluids, a maximum and minimum value was set for the amount of early and late cement at 75% and 25% (Case I in Table 3) and 87.5% and 12.5% (Case II in Table 3), respectively. For Case I, the composition of the early cement would have been $\delta^{13}\text{C} -47.5\text{‰}$ and $\delta^{18}\text{O} +0.8\text{‰}$ (Fig. 17) after correction for the detrital carbonate (Table 3). For Case II, these values would have been -40.9‰ and -0.8‰ , respectively. Considering that the early cement contains also

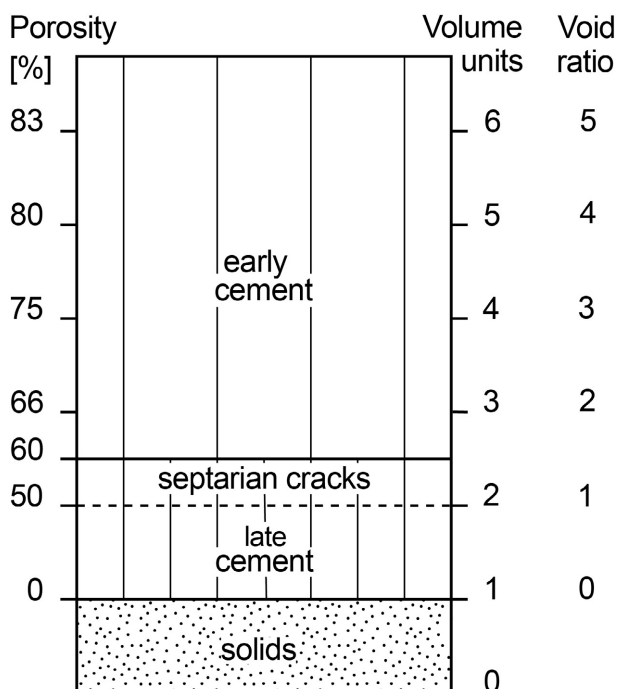


Fig. 16. Pore volume (given as porosity and void ratio) filled by different cement phases. The amount of late cement precipitated after septarian crack formation was estimated from cathodoluminescence microscopy and shrinkage limit tests (for details see text).

seawater-derived bicarbonate, the purely microbial-generated bicarbonate must have had the $\delta^{13}\text{C}$ composition even lighter than the

values calculated for both cases. The tight covariation of $\delta^{13}\text{C}$ and $\delta^{18}\text{O}$ values indicates that the contribution of seawater-derived bicarbonate component was rather constant during concreting growth. If it is tentatively assumed that the seawater-derived bicarbonate provided between 10% and 30% of the early cement, the purely microbial-generated bicarbonate in Case I would have had $\delta^{13}\text{C}$ values between -68.5‰ and -52.9‰ , and in Case II, $\delta^{13}\text{C}$ values would have been between -45.6‰ and -59.1‰ , respectively. Knowing that OSR produces bicarbonate with $\delta^{13}\text{C}$ ca -25‰ (Irwin *et al.*, 1977), that biogenic methane at modern seep sites exhibits $\delta^{13}\text{C}$ values mostly between -70‰ and -60‰ (e.g. Suess *et al.*, 1999; Faure *et al.*, 2010), and that AOM causes a slight ^{13}C depletion in the bicarbonate produced (Whiticar, 1999), results of these calculations confirm that AOM was the main source of bicarbonate prevailing over OSR.

Formation of radish concretions

Elongate radish concretions are morphologically similar to tubular concretions that formed along conduits of methane-charged fluids within the sulphate reduction zone (e.g. Nyman *et al.*, 2010; van de Schootbrugge *et al.*, 2010; Cavagna *et al.*, 2015). Such tubular conduit-related concretions support the above interpretation that radish concretions formed along fluid-flow structures. Conduit-related, tubular concretions,

Table 3. Isotopic composition of concretion body, cements and diagenetic fluids

(Bi)carbonate type	$\delta^{13}\text{C}$ (‰)	Relative proportion (%)	Proportion of total carbonate (%)
Concretion body (without septarian crack fill)	-35.0	100.0	100
Detrital carbonate	-2.5	3.0	3
Concretion body cement (without septarian crack fill)	-36.0	97.0	97
Case I – Concretion body cement (Early cement : late cement = 75 : 25)	-36.0	100.0	97
Late diagenetic cement*	-1.5	25.0	24
Early diagenetic cement*	-47.5	75.0	73
Case II – Concretion body cement (Early cement : late cement = 87.5 : 12.5)	-36.0	100.0	97
Late diagenetic cement*	-1.5	12.5	12
Early diagenetic cement*	-40.9	87.5	85

* 'Early diagenetic' and 'late diagenetic' refer to authigenic carbonate precipitated in the concretion body before and after formation of the septarian cracks, respectively.

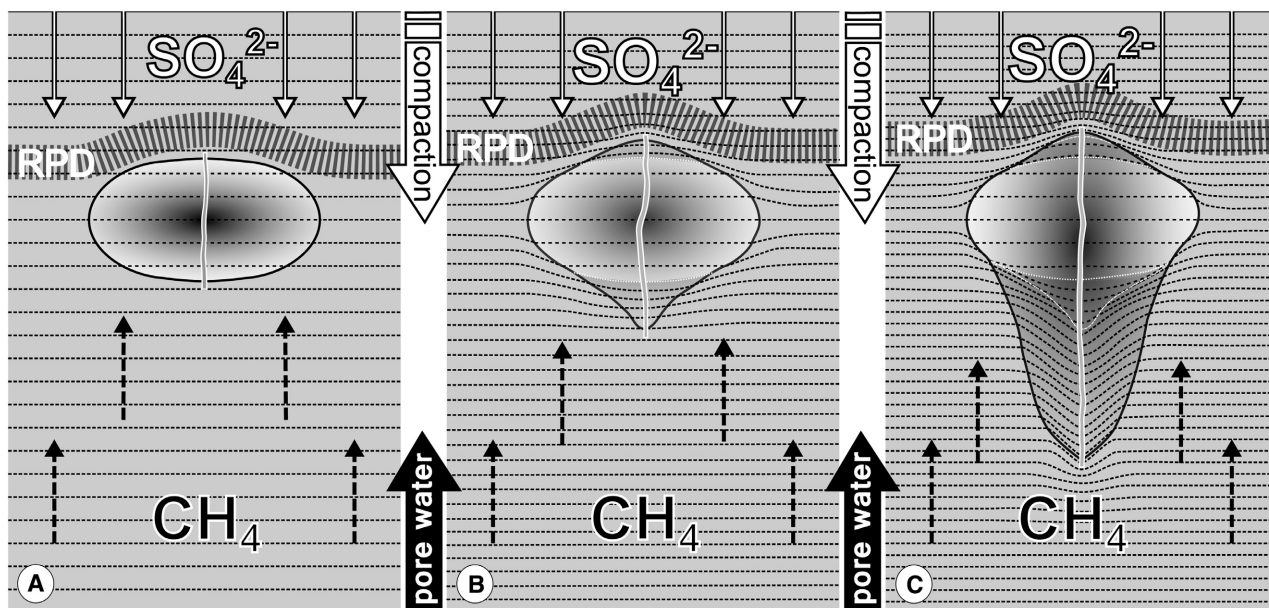


Fig. 17. Schematic representation of radish concretion formation (from left to right); sediment aggradation during concretion formation is not shown. (A) Initial stage, below the redox potential discontinuity (RPD) upward-migrating methane becomes anaerobically oxidized by reduction of sulphate supplied from above, while a central tube acted as fluid conduit. (B) Due to increasing overload, differential compaction affects host sediment that is deformed below and above the concretion and subsequently becomes partly incorporated into the growing concretion. (C) Final stage, due to further compaction and concretion growth additional increasingly deformed host sediment becomes part of the concretion. Formation of septarian cracks is not shown.

however, do not exhibit clear evidence of growth during compaction such as concretions from Jurassic mudrock in France: These concretions display the same architecture as the radish concretions of this study; with a central Fe-sulphide rich axial part surrounded by the concretion body which is cross-cut by septarian cracks, but the French concretions do not exhibit any inclined layers internally (van de Schootbrugge *et al.*, 2010, fig. 4C). Evidently, the conduit-related concretions became cemented around the axial tube before the host sediment experienced considerable compaction because of a high methane supply that resulted in more rapid growth than the radish concretions.

The radish concretions formed in highly porous mud around distinct dewatering structures that could be maintained as long as pore water was expelled out of the Opalinuston Formation mud underneath. Very likely, the present-day *ca* 80 m thick, lower muddy part of the Opalinuston Formation was underconsolidated for a considerable time because the increase in overburden due to rapid deposition (30 to 40 cm kyr⁻¹) exceeded the threshold value for

normal consolidation of *ca* 20 cm kyr⁻¹ (Einssele, 1977). Therefore, pore water was still moving upward although sediment accumulation had already slowed down. Both the thick, still delayed compacting and dewatering mud underneath and the slowly accumulating sediment above preconditioned the long-term growth of the radish concretions due to localized upward pore water migration. The occurrence of Fe-sulphide lined tubes similar to those acting as dewatering structures in modern sediments supports this hypothesis (Fig. 13) as they likely facilitated the supply of biogenic methane from below. Rather rapid delivery of methane into the sulphate reduction zone might have initiated the pervasive cementation of the parent domain (Fig. 17A). At that time, the sulphate–methane transition zone must have been located at a shallow sediment depth as recorded by the high initial porosity of 75 to 80% (e.g. Baldwin & Butler, 1985; Duck, 1995; Hong *et al.*, 2020). After the parent domain was pervasively cemented, the concretions grew only in a vertical direction, probably guided by the Fe-sulphide lined vertical tube while Fe-

sulphide and carbonate precipitated simultaneously (Fig. 17B and C). The small range of the bulk carbon and oxygen isotope values of the concretion body documents that geochemical conditions varied only little during the time when the radish concretion resided and grew within the sulphate–methane transition zone, and slow sediment accumulation on the seafloor did not affect these conditions. The pronounced asymmetry of the radish concretions is indicative of a considerable contribution of upward-migrating pore fluid (Raiswell, 1988) out of the compacting muddy Opalinuston Formation.

The growth of early diagenetic, ellipsoidal carbonate concretions has been calculated by diffusion equations to be in the range of several thousands to a few tens of thousands of years depending on their size (Raiswell & Fisher, 2004; Blouet *et al.*, 2021). Therefore, the long-term formation of radish concretions appears to have been facilitated by recurrent sediment reworking and slow net-deposition that might have lasted for up to 2.5 Myr, as suggested by the geohistory analysis (Fig. 15).

The concretions remained in an incompletely lithified/cemented, plastic state as recorded by the presence of narrowing-outward septarian cracks (Wetzel, 1992; see above). Similarly, poorly lithified concretions occur in modern sediments at methane seep sites (Franchi *et al.*, 2017) or within Holocene estuarine deposits (Wetzel *et al.*, 2017), respectively. These findings agree with petrographic studies of concretions from various formations revealing that early and late diagenetic cements co-occur within concretions (see Mozley, 1996; and references therein). Therefore, it is justifiable to consider that the body of radish concretions contains a mixture of early and late diagenetic cement precipitated before and after formation of septarian cracks, respectively.

Although organic-rich mud generating microbial methane and having been affected by pronounced fluctuations in deposition rate occur widely in various basins, the presence of radish concretions is not observed often. Their rare occurrence is probably due to the very peculiar conditions required for their formation. During the prolonged span of time when mud is undergoing considerable compaction due to seafloor deposition; radish concretions need to reside within the sulphate–methane transition zone, which is typically 1 m or less in thickness (e.g. Pohlmann *et al.*, 2013) where the flux of

methane from below is balanced by sulphate supply from above. Downward transfer of sulphate is affected by: (i) sedimentation rate increasing the distance between the seafloor and the depth at which concretions occur; and (ii) deposition of organic matter which leads to consumption of sulphate. If one of these factors is too high, the sulphate–methane transition zone migrates upward as it does if methane flux increases (e.g. Whiticar, 2002). If the transition zone migrates upward, an initially cemented parent domain of a concretion can no longer grow, and it is preserved in the rock record as an ellipsoidal concretion. At a high methane flux, the sulphate–methane transition zone tends to thin (e.g. Regnier *et al.*, 2011) and tubular concretions traverse it completely and form rather rapidly, similar to what occurs at methane seep sites. Thus, it is highly unlikely that sediment deformed by compaction is incorporated into these tubular concretions. Nonetheless, in all cases, the compaction behaviour of the host mud can be estimated from the minus-cement porosity of the parent domain that allows (re-)constructing of a porosity–depth path of the host sediment and relating concretion growth to burial depth.

If septarian cracks are present, the minimum depth of their formation can be estimated from the minus-cement porosity at the crack's tips. If cracks exhibit the typical features of shrinkage phenomena, there was still porosity left open within the concretion body after crack formation wherein cement could precipitate and also fill the cracks. The shrinkage behaviour of the host mud provides an upper limit for the porosity available when cracks formed.

CONCLUSIONS

1 Radish concretions typically exhibit a columnar to pear-shaped, stipe-down geometry that developed when they grew during compaction within early Aalenian muddy host sediment. Around a Fe-sulphide lined tube, an initial parent domain became pervasively cemented at a minus-cement porosity of 75 to 80% that corresponds to a shallow sediment depth of 5 to 10 m or less. The parent domain acted as a relatively rigid body when the host mud further compacted during burial and, hence, the increasing overburden resulted in active earth pressure at the base and passive

earth pressure at the top of the growing concretion. The resulting stresses modulated the deformation of the sedimentary laminae above and below the concretion, which became inclined and later incorporated into the concretions.

2 Simultaneous precipitation of carbonate and Fe-sulphide as well as the bulk C and O isotope data demonstrate that the radish concretions grew within the sulphate reduction zone wherein anaerobic oxidation of methane (AOM) and organoclastic material (OSR) occurred while sulphate was reduced. These microbially mediated reactions lasted for a prolonged time period of up to 2.5 Myr. This was possible because sediment net-aggradation in the study area was low (<2 to 3 cm kyr⁻¹) during the late Aalenian and early Bajocian and, hence, the interval wherein the concretions were growing could reside within the sulphate reduction zone.

3 Concretion growth continued for such a long time because the compaction of the present-day 120 m thick, rapidly accumulated, grey mudrock containing 0.5 to 2.5% C_{org} underneath was retarded due to its low permeability that in turn conditioned a long-term active, but slow, compaction flow. This provided methane for a long period of time.

4 Concretion growth ceased, because sulphate supply declined due to increasing distance to the seafloor and decreasing permeability of the cover sediment. The decay of the AOM-related and OSR-related microbial biomass could have caused the formation of septarian cracks at a burial depth of about 50 to 70 m.

5 The narrowing-outward septarian cracks indicate that the concretion body was still in a plastic state when the cracks formed. Because the cracks terminate in concretion domains having a minus-cement porosity of 60%, the pore volume still open after septarian crack formation is estimated to have been in the range of 25%. Because the septarian cracks did not reach the concretion surface they were filled by cement provided by ions diffusing or migrating within water films along grain boundaries or within micropores through the concretion body. Therefore, cement filling the septarian cracks could also precipitate in open pores of the concretion body as evidenced by its dull cathodoluminescence colour and relatively light back-scattered electron colour related to increased Fe²⁺ content. Consequently, it is difficult to interpret centre-to-edge changes in terms of evolving diagenetic changes.

6 Considering the amount and composition of this late diagenetic cement (precipitated after septarian crack formation), the fluid providing the early diagenetic cement (precipitated before septarian crack formation) had, prior to mixing with seawater, a $\delta^{13}\text{C}$ composition, (assuming that seawater-derived bicarbonate accounted for 10 to 30% of early diagenetic cement) ranging between ca -45‰ and -70‰, which indicates that it was chiefly derived from AOM prevailing over OSR.

REPOSITORY

Most specimens shown in the figures are stored at the Museum of Natural History Basel (NMB) with the following access numbers: Figs 4A, 5, 10 (AA 4021); Fig. 4C (AA 4022), Fig. 6 (AA 4023); and Fig. 7B (AA 4024).

ACKNOWLEDGEMENTS

The radish and columnar concretions were discovered and collected during a rainy, but nonetheless very exciting, field trip in 1981 with the late A. Seilacher (Tübingen, Germany). The geochemical data were provided by several colleagues; the carbonate content was measured by M. Wiesner (Hamburg, Germany), carbon and oxygen isotopes were determined by S. Bernasconi (ETH Zürich, Switzerland) and T. Kuhn (Basel). Associate Editor J. Hendry (Dublin, Ireland) as well as reviewers A. Immenhauser (Bochum, Germany) and R. Raiswell (Leeds, UK) provided constructive and helpful comments and suggestions that improved the manuscript considerably. All of these contributions are gratefully acknowledged. This research did not receive any specific grant from funding agencies in the public, commercial, or not-for-profit sectors.

DATA AVAILABILITY STATEMENT

Data available on request from the authors.

REFERENCES

- Al-Khafaji, A.W.N., Andersland, O.B. and ASCE Members. (1992) Equations for compression index approximation. *Journal of Geotechnical Engineering*, **118**, 148–153.
- Allia, V. (1996) *Sedimentologie und Ablagerungsgeschichte des Opalinustons in der Nordschweiz*. Dissertationen aus

- dem Geologisch-Paläontologischen Institut der Universität Basel, No. 10, 185 pp.
- Allison, P.** and **Pye, K.** (1994) Early diagenetic mineralization and fossil preservation in modern carbonate concretions. *Palaos*, **9**, 561–575.
- Anderson, T.F.** and **Arthur, M.A.** (1983) Stable isotopes of oxygen and carbon and their application to sedimentologic and paleoenvironmental problems. In: *Stable Isotopes in Sedimentary Geology* (Ed. Arthur, M.A.). Society of Economic Paleontologists and Mineralogists, Short Course Notes, **10**, 1-1–1-151.
- Athy, L.F.** (1930) Density, porosity, and compaction of sedimentary rocks. *Am. Assoc. Petrol. Geol. Bull.*, **14**, 1–24.
- Baldwin, B.** and **Butler, C.O.** (1985) Compaction curves. *Am. Assoc. Petrol. Geol. Bull.*, **69**, 622–626.
- Barnes, R.O.** and **Goldberg, E.D.** (1976) Methane production and consumption in anoxic marine sediments. *Geology*, **4**, 297–300.
- Bathurst, R.G.C.** (1975) *Carbonate Sediments and Their Diagenesis*, 2nd edn. Elsevier, Amsterdam, 658 pp.
- Bayer, U.** and **Wetzel, A.** (1989) Compactional behavior of fine-grained sediments – examples from Deep Sea Drilling Project cores. *Geol. Rundsch.*, **78**, 807–819.
- Blome, C.D.** and **Albert, N.R.** (1985) Carbonate concretions: an ideal sedimentary host for microfossils. *Geology*, **13**, 212–215.
- Blouet, J.-P., Arndt, S., Imbert, P.** and **Regnier, P.** (2021) Are seep carbonates quantitative proxies of CH₄ leakage? Modeling the influence of sulfate reduction and anaerobic oxidation of methane on pH and CaCO₃ saturation. *Chem. Geol.*, **577**, 120254.
- de Boever, E., Swennen, R.** and **Dimitrov, L.** (2006) Lower Eocene carbonate cemented chimneys (Varna, NE Bulgaria): Formation mechanisms and the (a)biological mediation of chimney growth? *Sed. Geol.*, **185**, 159–173.
- Bojanowski, M.J.** (2012) Geochemical paleogradient in pore waters controlled by AOM recorded in an Oligocene laminated limestone from the Outer Carpathians. *Chem. Geol.*, **292–293**, 45–56.
- Bojanowski, M.J., Barczuk, A.** and **Wetzel, A.** (2014) Deep-burial alteration of early-diagenetic carbonate concretions formed in Palaeozoic deep-marine greywackes and mudstones (Bardo Unit, Sudetes Mountains, Poland). *Sedimentology*, **61**, 1211–1239.
- Bojanowski, M.J., Ciurej, A., Haczeński, G., Jokubauskas, P., Schouten, S., Tyszka, J.** and **Bijl, P.K.** (2018) The Central Paratethys during Oligocene as an ancient counterpart of the present-day Black Sea: unique records from the coccolith limestones. *Mar. Geol.*, **403**, 301–328.
- Burdige, D.J.** (2006) *Geochemistry of Marine Sediments*. Princeton University Press, Princeton, NJ, 609 pp.
- Busch, W.H.** and **Keller, G.H.** (1981) The physical properties of Peru-Chile continental margin sediments – the influence of coastal upwelling on sediment properties. *J. Sediment. Petrol.*, **51**, 705–719.
- Campetella, D.M., Carmona, N.B., Ponce, J.J., Wetzel, A., Rodríguez, M.** and **Parada, M.N.** (2020) Trace fossils as tools to unravel oxygen conditions: a case study from Los Molles Formation (Toarcian-lower Callovian). *Revista de la Asociación Geológica Argentina*, **77**, 463–477.
- Canfield, D.E.** and **Raiswell, R.** (1991) Carbonate precipitation and dissolution – its relevance to fossil preservation. In: *Taphonomy: Releasing the Data Locked in the Fossil Record* (Eds. Allison, P. and Briggs, D.E.G.), pp. 411–453. Plenum, New York.
- Cavagna, S., Clari, P., Dela Pierre, F., Martire, L.** and **Natalicchio, M.** (2015) Sluggish and steady focussed flows through fine-grained sediments: the methane-derived cylindrical concretions of the Tertiary Piedmont Basin (NW Italy). *Mar. Petrol. Geol.*, **66**, 596–605.
- Claypool, G.E.** and **Kaplan, I.R.** (1974) The origin and distribution of methane in marine sediments. In: *Natural Gases in Marine Sediments* (Ed. Kaplan, I.R.), pp. 99–139. Plenum, New York.
- Coleman, M.L.** and **Raiswell, R.** (1993) Microbial mineralization of organic matter: mechanisms of self-organization and inferred rates of precipitation of diagenetic minerals. *Philosophical Transactions of the Royal Society London, Series A*, **344**, 69–87.
- Day-Stürat, R.J., Loucks, R.G., Milliken, K.L., Hillier, S.** and **van der Pluijm, B.A.** (2008) Phyllosilicate orientation demonstrates early timing of compactional stabilization in calcite-cemented concretions in the Barnett Shale (Late Mississippian), Fort Worth Basin, Texas (U.S.A.). *Sed. Geol.*, **208**, 27–35.
- Dera, G., Brigaud, B., Monna, F., Laffont, R., Pucéat, E., Deconinck, J.-F., Pellenard, P., Joachimski, M.M.** and **Durlet, C.** (2011) Climatic ups and downs in a disturbed Jurassic world. *Geology*, **39**, 215–218.
- Dietze, V., Gräbenstein, S., Franz, M., Schweigert, G.** and **Wetzel, A.** (2021) The Middle Jurassic Opalinuston formation (Aalenian, Opalinum Zone) at its type locality near Bad Boll and adjacent outcrops (Swabian Alb, SW Germany). *Palaeodiversity*, **14**, 15–115.
- DIN 18122-2.** (2000) *Baugrund-Untersuchung von Bodenproben: Zustandsgrenzen (Konsistenzgrenzen) – Teil 2: Bestimmung der Schrumpfgrenze*. Beuth, Berlin, pp. 10.
- Dix, G.R.** and **Mullins, H.T.** (1987) Shallow, subsurface growth and burial alteration of Middle Devonian concretions. *J. Sediment. Petrol.*, **57**, 140–152.
- Duck, R.W.** (1995) Subaqueous shrinkage cracks and early sediment fabrics preserved in Pleistocene calcareous concretions. *J. Geol. Soc. London*, **152**, 151–156.
- Durga Prasada Rao, N., Srihari, Y.** and **Behairy, A.** (1982) Columnar concretions in the Visakhapatnam red sediments on the east coast of India. *Sed. Geol.*, **31**, 303–316.
- Einsele, G.** (1977) Range, velocity, and material flux of compaction flow in growing sedimentary sequences. *Sedimentology*, **24**, 639–655.
- Einsele, G.** and **Kelts, K.** (1982) Pliocene and Quaternary mud turbidites in the Gulf of California: sedimentology, mass physical properties and significance. *Init. Rep. Deep Sea Drilling Proj.*, **64 Part 2**, 511–528.
- Elie, M.** and **Mazurek, M.** (2008) Biomarker transformations as constraints for the depositional environment and for maximum temperatures during burial of Opalinus Clay and Posidonia Shale in northern Switzerland. *Appl. Geochem.*, **23**, 3337–3354.
- Faure, K., Greinert, J., Schneider von Deimling, J., McGinnis, D.F., Kipfer, R.** and **Linke, P.** (2010) Methane seepage along the Hikurangi Margin of New Zealand: geochemical and physical data from the water column, sea surface and atmosphere. *Mar. Geol.*, **272**, 170–188.
- Franchi, F., Rovere, M., Gamberi, F., Rashed, H., Vaselli, O.** and **Tassi, F.** (2017) Authigenic minerals from the Paola Ridge (southern Tyrrhenian Sea): evidence of episodic methane seepage. *Mar. Petrol. Geol.*, **86**, 228–247.
- Franz, M.** and **Nitsch, E.** (2009) Zur lithostratigraphischen Gliederung des Aalenium in Baden-Württemberg. *LGRB-Informationen (Landesamt für Geologie, Rohstoffe und Bergbau)*, **22**, 123–146.

- geotechdata.** (2013) *Soil friction angle*. <http://www.geotechdata.info/parameter/angle-of-friction.html> (accessed 15 Nov 2015).
- Geyer, O.F. and Gwinner, M.P.** (2011) *Geologie von Baden-Württemberg*. Schweizerbart, Stuttgart, 627 pp.
- Hall, J.T. and Savrda, C.E.** (2008) Ichnofossils and ichnofabrics in syngenetic phosphatic concretions in siliciclastic shelf deposits, Ripley Formation, Cretaceous, Alabama. *Palaios*, **23**, 233–245.
- Hardenbol, J., Thierry, J., Farley, M.B., Jacquin, T., de Graciansky, P.-C. and Vail, P.** (1998) Mesozoic and Cenozoic sequence chronostratigraphic framework of European basins. In: *Mesozoic and Cenozoic Sequence Stratigraphy of European Basins* (Eds P.-C. de Graciansky, J. Hardenbol, T. Jacquin and P. Vail), *SEPM (Society for Sedimentary Geology) Special Publications*, **60**, pp. 3–13 (+ 8 charts).
- Hendry, J.P., Pearson, M.J., Trewin, N.H. and Fallicks, A.E.** (2006) Jurassic septarian concretions from NW Scotland record interdependent bacterial, physical and chemical processes of marine mudrock diagenesis. *Sedimentology*, **53**, 537–565.
- Hesselbo, S.P. and Palmer, T.J.** (1992) Reworked early diagenetic concretions and the bioerosional origin of a regional discontinuity within the British Jurassic marine mudstones. *Sedimentology*, **39**, 1045–1065.
- van Hinte, J.E.** (1978) Geohistory analysis – application of micropaleontology in exploration geology. *Am. Ass. Petrol. Geol. Bull.*, **62**, 201–222.
- Hong, B., Li, X., Wang, L., Li, L., Xue, Q. and Meng, J.** (2020) Using the effective void ratio and specific surface area in the Kozeny-Carman equation to predict the hydraulic conductivity of loess. *Water*, **12**, 24.
- Hudson, J.D.** (1978) Concretions, isotopes and diagenetic history of the Oxford Clay (Jurassic) of central England. *Sedimentology*, **25**, 339–370.
- Hudson, J.D., Coleman, M.L., Barreiro, B.A. and Hollingworth, N.T.J.** (2001) Septarian concretions from the Oxford Clay (Jurassic, England, UK): involvement of original marine and multiple external pore fluids. *Sedimentology*, **48**, 507–531.
- Irwin, H., Curtis, C. and Coleman, M.** (1977) Isotopic evidence for the source of diagenetic carbonates formed during burial of organic-rich sediments. *Nature*, **269**, 209–213.
- Izdebska-Mucha, D. and Wójcik, E.** (2013) Testing shrinkage factors: comparison of methods and correlation with index properties of soils. *Bull. Eng. Geol. Environ.*, **72**, 15–24.
- James, W.C.** (1985) Early diagenesis, Atherton formation (Quaternary): a guide for understanding early cement distribution and grain modifications in nonmarine deposits. *J. Sediment. Petrol.*, **55**, 135–146.
- Keller, G.** (1982) Organic matter and the geotechnical properties of submarine sediments. *Geo-Mar. Lett.*, **2**, 191–198.
- Lash, G.G.** (2018) Significance of stable carbon isotope trends in carbonate concretions formed in association with anaerobic oxidation of methane (AOM), Middle and Upper Devonian shale succession, western New York State, USA. *Mar. Petrol. Geol.*, **91**, 470–479.
- Lash, G.G. and Blood, D.** (2004) Geochemical and textural evidence for early (shallow) diagenetic growth of stratigraphically confined carbonate concretions, Upper Devonian Rhinestreet black shale, western New York. *Chem. Geol.*, **206**, 407–424.
- Lee, H.J.** (1973) Measurements and estimates of engineering and other physical properties, Leg 19. *Init. Rep. Deep Sea Drilling Proj.*, **19**, 897–901.
- Leonowicz, P.** (2015) Ichnofabrics of shallow-marine mudstone, the result of changing environmental conditions: an example from the Middle Jurassic ore-bearing clay from southern Poland. *Facies*, **61**, 11.
- Lippmann, F.** (1955) Ton, Geoden und Minerale des Barrême von Hoheneggelsen. *Geol. Rundsch.*, **43**, 475–503.
- Loyd, S. J. and Berelson, W. M.** (2016) The modern record of "concretionary" carbonate: reassessing a discrepancy between modern sediments and the geologic record. *Chem. Geol.*, **420**, 77–87.
- Löwemark, L.** (2003) Automatic image analysis of X-ray radiographs: a new method for ichnofabric evaluation. *Deep-Sea Res. I*, **50**, 815–827.
- Machel, H.G.** (1985) Cathodoluminescence in calcite and dolomite and its chemical interpretation. *Geosci. Can.*, **12**, 139–147.
- Mavromatis, V., Botz, R., Schmidt, M., Liebetrau, V. and Hensen, C.** (2014) Formation of carbonate concretions in surface sediments of two mud mounds, offshore Costa Rica: a stable isotope study. *Int. J. Earth Sci.*, **103**, 1831–1844.
- Mazurek, M., Hurford, A.J. and Leu, W.** (2006) Unravelling the multi-stage of the Swiss Molasse Basin: integration of apatite fission track, vitrinite reflectance and biomarker isomerisation analysis. *Basin Res.*, **18**, 27–50.
- McBride, E.F., Picard, M.D. and Milliken, K.L.** (2003) Calcite-cemented concretions in Cretaceous sandstone, Wyoming and Utah, USA. *J. Sediment. Res.*, **73**, 462–483.
- Melezhik, V.A., Fallick, A.E., Smith, R.A. and Rosse, D.M.** (2007) Spherical and columnar, septarian, ¹⁸O-depleted, calcite concretions from Middle-Upper Permian lacustrine siltstones in northern Mozambique: evidence for very early diagenesis and multiple fluids. *Sedimentology*, **54**, 1389–1416.
- Mitchell, J.K.** (1993) *Fundamentals of Soil Behavior*. Wiley & Sons, New York, 437 pp.
- Mozley, P.S.** (1996) The internal structure of carbonate concretions in mudrocks: a critical evaluation of the conventional concentric model of concretion growth. *Sed. Geol.*, **103**, 85–91.
- Mozley, P.S. and Burns, S.J.** (1993) Oxygen and carbon isotopic composition of marine carbonate concretions: an overview. *J. Sediment. Petrol.*, **63**, 73–83.
- Nyman, S.L., Nelson, C.S. and Campbell, K.A.** (2010) Miocene tubular concretions in East Coast Basin, New Zealand: analogue for subsurface plumbing of cold seeps. *Mar. Geol.*, **272**, 319–336.
- Oertel, G. and Curtis, C.D.** (1972) Clay-ironstone concretion preserving fabrics due to progressive compaction. *Geol. Soc. Am. Bull.*, **83**, 2597–2606.
- Pohlmann, J.W., Riedel, M., Bauer, J.E., Canuel, E.A., Paull, C.K., Lapham, L., Grabowski, K.S., Coffin, R.B. and Spence, G.D.** (2013) Anaerobic methane oxidation in low-organic content methane seep sediments. *Geochim. Cosmochim. Acta*, **108**, 184–201.
- Raiswell, R.** (1988) Evidence for surface reaction-controlled growth of carbonate concretions in shales. *Sedimentology*, **35**, 571–575.
- Raiswell, R. and Canfield, D.E.** (2012) The iron biogeochemical cycle past and present. *Geochemical Perspectives*, **1**, 1–220.
- Raiswell, R. and Fisher, Q.j.** (2000) Mudrock-hosted carbonate concretions: a review of growth mechanisms

- and their influence on chemical and isotopic composition. *J. Geol. Soc.*, **157**, 239–251.
- Raiswell, R.** and **Fisher, Q.J.** (2004) Rates of carbonate cementation associated with sulphate reduction in DSDP/ODP sediments: implications for the formation of concretions. *Chem. Geol.*, **211**, 71–85.
- Regnier, P., Dale, A.W., Arndt, S., LaRowe, D.E., Mogollón, J.** and **Van Cappellen, P.** (2011) Quantitative analysis of anaerobic oxidation of methane (AOM) in marine sediments: a modelling perspective. *Earth-Science Reviews*, **106**, 105–130.
- Rieke, H.H.I.** and **Chilingarian, G.V.** (1974) *Compaction of Argillaceous Sediments*. Developments in Sedimentology, 16. Elsevier, Amsterdam, 424 pp.
- Sass, E., Bein, A.** and **Almogi-Labin, A.** (1991) Oxygen-isotope composition of diagenetic calcite in organic-rich rocks: evidence from ^{18}O depletion in marine anaerobic pore water. *Geology*, **19**, 839–842.
- Schmidt, R.** (1996) *Feinstratigraphie des Opalinustons (Dogger alpha) der mittleren Schwäbischen Alb, Baden-Württemberg*. Planetary Stratigraphy, Series E, No. 1. Edition Schmidt, Tübingen, 110 pp.
- van de Schootbrugge, B., Harazim, D., Sorichter, K., Oschmann, W., Fiebig, J., Püttmann, W., Peinl, M., Zanella, F., Teichert, B.M.A., Hoffmann, J., Stadnitskaia, A.** and **Rosenthal, Y.** (2010) The enigmatic ichnofossil *Tisooa siphonalis* and widespread authigenic seep carbonate formation during the Late Pliensbachian in southern France. *Biogeosciences*, **7**, 3123–3138.
- Seilacher, A.** (2001) Concretion morphologies reflecting diagenetic and epigenetic pathways. *Sed. Geol.*, **143**, 41–57.
- Sellés-Martínez, J.** (1996) Concretion morphology, classification and genesis. *Earth Sci. Rev.*, **41**, 177–210.
- Snyder, G.T., Hiruta, A., Matsumoto, R., Dickens, G.R., Tomaru, H., Takeuchi, R., Komatsubara, J., Ishida, Y.** and **Yu, H.** (2007) Pore water profiles and authigenic mineralization in shallow marine sediments above the methane-charged system on Umitaka Spur, Japan Sea. *Deep-Sea Res. II*, **54**, 1216–1239.
- Šrámek, J.** (1978) Relative age of diagenetic carbonate concretions in relation to the sediment porosity. *Acta Universitatis Carolinae – Geologica*, **1978**, 307–321.
- Suess, E., Torres, M.E., Bohrmann, G., Collier, R.W., Greinert, J., Linke, P., Rehder, G., Trehu, A., Wallmann, K., Winckler, G.** and **Zuleger, E.** (1999) Gas hydrate destabilization: enhanced dewatering, benthic material turnover and large methane plumes at the Cascadia convergent margin. *Earth Planet. Sci. Lett.*, **170**, 1–15.
- Swart, P.K.** (2015) The geochemistry of carbonate diagenesis: past, present, and future. *Sedimentology*, **62**, 1233–1304.
- Taylor, K.G.** and **Macquaker, J.H.S.** (2000) Early diagenetic pyrite morphology in a mudstone-dominated succession: the Lower Jurassic Cleveland Ironstone Formation, eastern England. *Sed. Geol.*, **131**, 77–86.
- Thaler, C., Katz, A., Bonifacie, M., Ménez, B.** and **Ader, M.** (2020) Oxygen isotope composition of waters recorded in carbonates in strong clumped and oxygen isotopic disequilibrium. *Biogeosciences*, **17**, 1731–1744.
- Tucker, M.E.** and **Wright, V.P.** (1990) *Carbonate Sedimentology*. Blackwell, Oxford, London, 482 pp.
- Villagómez-Díaz, D., Omodeo-Salé, S., Ulyanov, A.** and **Moscariello, A.** (2021) Insights into the thermal history of north-eastern Switzerland – apatite fission track dating of deep drill core samples from the Swiss Jura Mountains and the Swiss Molasse Basin. *Geosciences*, **11**, 10.
- Voellmy, A.** (1937) *Eingebettete Rohre*. Dissertation ETH Zürich, Zürich, 151 pp.
- Wangen, M.** (2010) *Physical Principles of Sedimentary Basin Analysis*. Cambridge University Press, Cambridge, 527 pp.
- Weaver, P.P.E.** and **Schultheiss, P.J.** (1983) Vertical open burrows in deep-sea sediments 2 m in length. *Nature*, **301**, 329–331.
- Wetzel, A.** (1981) Ökologische und stratigraphische Bedeutung biogener Gefüge in quartären Sedimenten am NW-afrikanischen Kontinentalrand. "Meteor" Forschungs-Ergebnisse, Reihe C, **34**, 1–47.
- Wetzel, A.** (1983) Biogenic structures in modern slope to deep-sea sediments in the Sulu Sea Basin (Philippines). *Palaeogeogr. Palaeoclimatol. Palaeoecol.*, **42**, 285–304.
- Wetzel, A.** (1990) Interrelationships between porosity and other geotechnical properties of slowly deposited, fine-grained marine surface sediments. *Mar. Geol.*, **92**, 105–113.
- Wetzel, A.** (1992) An apparent concretionary paradox. *Zentralblatt für Geologie und Paläontologie, Teil I*, **1991**, 2823–2830.
- Wetzel, A.** and **Allia, V.** (2000) The significance of hiatus beds in shallow-water mudstones: an example from the Middle Jurassic of Switzerland. *J. Sediment. Res.*, **70**, 170–180.
- Wetzel, A.** and **Allia, V.** (2003) Der Opalinuston in der Nordschweiz: Lithologie und Ablagerungsgeschichte. *Eclogae Geol. Helv.*, **96**, 451–469.
- Wetzel, A.** and **Meyer, C.A.** (2006) The dangers of high-rise living on a muddy seafloor: an example of crinoids from shallow-water mudstones (Aalenian, northern Switzerland). *Palaios*, **21**, 155–167.
- Wetzel, A.** and **Reisdorf, A.G.** (2007) Ichnofabrics elucidate the accumulation history of a condensed interval containing a vertically emplaced ichthyosaur skull. In: *Sediment-Organism Interactions: A Multifaceted Ichnology* (Eds R.G. Bromley, L.A. Buatois, M.G. Mángano, J.F. Genise and R.N. Melchor), SEPM Special Publications, **88**, pp. 241–251.
- Wetzel, A., Szczygielski, A., Unverricht, D.** and **Stattegger, K.** (2017) Sedimentological and ichnological implications of rapid Holocene flooding of a gently sloping mud-dominated incised valley – an example from the Red River (Gulf of Tonkin). *Sedimentology*, **64**, 1173–1202.
- Wetzel, A., Tjallingii, R.** and **Wiesner, M.G.** (2011) Bioturbational structures record environmental changes in the upwelling area off Vietnam (South China Sea) for the last 150,000 years. *Palaeogeogr. Palaeoclimatol. Palaeoecol.*, **311**, 256–267.
- Wheeler, A.J.** and **Stadnitskaia, A.** (2011) Benthic deep-sea carbonates: reefs and seeps. In: *Deep-Sea Sediments* (Eds H. Hüneke and T. Mulder), *Developments in Sedimentology*, **63**, pp. 397–455. Elsevier, Amsterdam.
- Whiticar, M.J.** (1999) Carbon and hydrogen isotope systematics of bacterial formation and oxidation of methane. *Chem. Geol.*, **161**, 291–314.
- Whiticar, M.** (2002) Diagenetic relationships of methanogenesis, nutrients, acoustic turbidity, pockmarks and freshwater seepages in Eckernförde Bay. *Mar. Geol.*, **182**, 29–53.
- Zatoń, M., Machocka, S., Wilson, M.A., Marynowski, L.** and **Taylor, P.D.** (2011) Origin and paleoecology of Middle Jurassic hiatus concretions from Poland. *Facies*, **57**, 275–300.

Manuscript received 31 December 2020; revision accepted 17 June 2021